AD_____
(Leave blank)

Award Number: W81XWH-10-1-0743

TITLE: A Novel Multivoxel-Based Quantitation of Metabolites and Lipids Noninvasively Combined with Diffusion-Weighted Imaging in Breast Cancer

PRINCIPAL INVESTIGATOR: Michael Albert Thomas Ph.D.

CONTRACTING ORGANIZATION:

The Regents of the University of California
Los Angeles, CA 90024-1406

REPORT DATE: 1 OCT 2013

TYPE OF REPORT: Annual

PREPARED FOR: U.S. Army Medical Research and Materiel Command
               Fort Detrick, Maryland 21702-5012

DISTRIBUTION STATEMENT:

    Approved for public release; distribution unlimited

The views, opinions and/or findings contained in this report are those of the author(s) and should not be construed as an official Department of the Army position, policy or decision unless so designated by other documentation.

REPORT DOCUMENTATION PAGE

1. REPORT DATE	2. REPORT TYPE	3. DATES COVERED
1 OCT 2013	ANNUAL	1 SEPT 2012-31 AUG 2013

4. TITLE AND SUBTITLE

A Novel Multivoxel-Based Quantitation of Metabolites and Lipids Noninvasively Combined with Diffusion-Weighted Imaging in Breast Cancer

5a. CONTRACT NUMBER

5b. GRANT NUMBER
W81XWH-10-1-0743

5c. PROGRAM ELEMENT NUMBER

6. AUTHOR(S)

Michael Albert Thomas Ph.D

athomas@mednet.ucla.edu

5d. PROJECT NUMBER

5e. TASK NUMBER

5f. WORK UNIT NUMBER

7. PERFORMING ORGANIZATION NAME(S) AND ADDRESS(ES)

The Regents of the University of California
Los Angeles, CA 90024-1406

8. PERFORMING ORGANIZATION REPORT NUMBER

9. SPONSORING / MONITORING AGENCY NAME(S) AND ADDRESS(ES)
U.S. Army Medical Research and Materiel Command
Fort Detrick, Maryland 21702-5012

10. SPONSOR/MONITOR'S ACRONYM(S)

11. SPONSOR/MONITOR'S REPORT NUMBER(S)

12. DISTRIBUTION / AVAILABILITY STATEMENT
Approved for Public Release; Distribution Unlimited

13. SUPPLEMENTARY NOTES

14. ABSTRACT
To extend the single-voxel based 2D MRS version of L-COSY to multi-voxel based analogue on a 3T MRI/MRS scanner using the echo-planar imaging (EPI) based spatial encoding for determining metabolic distributions over many voxels, ii) To implement a Matlab-based post-processing algorithm in order to process the 2D COSY data recorded in breast cancer, iii) To record DWI and to calculate ADC maps in breast cancer patients and healthy controls, and iv) To correlate the changes in metabolite and lipid levels with ADC changes in breast cancer patients and healthy women. Scope: A major outcome will demonstrate improving the specificity of malignant and benign tumors . Improved imaging techniques will enable unambiguous measurement of metabolites and the lipids in situ, which could potentially complement the existing diagnostic modalities commonly used in breast carcinoma. Major Findings: The MR protocol including 4D EP-COSI and DWI-MRI was successfully evaluated in six healthy women, 3 benign and 4 malignant breast cancer patients on a 3T MRI scanner. Report of the Progress: 4D EP-COSI and DWI-MRI were recorded in 13 subjects:4 malignant and 3 benign breast cancer patients and 6 healthy women. The EP-COSI data showed water and lipid/metabolite changes with DWI images showing reduced ADC values in suspicious lesions of breast cancer patients compared to healthy women.

15. SUBJECT TERMS Magnetic resonance imaging, magnetic resonance spectroscopy, echo planar correlated spectroscopic imaging, diffusion weighted imaging, apparent diffusion coefficient, choline, lipids, water, saturated and unsaturated lipids

16. SECURITY CLASSIFICATION OF:			17. LIMITATION OF ABSTRACT	18. NUMBER OF PAGES	19a. NAME OF RESPONSIBLE PERSON USAMRMC
a. REPORT	b. ABSTRACT	c. THIS PAGE			
U	U	U	UU	26	19b. TELEPHONE NUMBER *(include area code)*

Table of Contents

Introduction:

A leading cause of cancer deaths among women worldwide is due to breast cancer and new therapies and optimal treatments are continuously being conceived and explored to better control or even cure this disease. (1). Diagnosis and therapeutic management of the breast tumor remain significant medical challenges, hence early detection, diagnosis, and timely treatments are essential to successful health care (2). Magnetic resonance imaging and spectroscopy (MRI/MRS) have gained significant importance during the last fifteen years for the diagnosis and monitoring of breast cancer therapy. The sensitivity of MRI/MRS for anatomical delineation is very high and the consensus is that MRI is more sensitive in detection than x-ray mammography. Advantages of MRS include delivery of biochemical information about tumor metabolism, which can potentially assist in the staging of cancers and monitoring responses to treatment. High sensitivity is a major advantage of contrast enhanced MRI, but its diagnostic relevance in the future will largely depend on improvements in specificity. Current approaches in the application of MRI to breast tumors aim to improve specificity and sensitivity (4-17). Increased specificity is necessary to reduce the number of biopsies performed to confirm false positive findings. Diffusion-weighted imaging (DWI) is another MR based technique that probes the microstructure of tissues and is sensitive to the degree to which motion of water molecules is restricted in relation to how packed together cells are (17, 18). It has been reported that high resolution DWI may add valuable functional information to conventional MR protocols with short measurement times for the diagnosis of breast cancer and improve the specificity of MR imaging (19-21). However, new technological developments are necessary to assess their role in breast diagnosis. A method capable of identifying biochemical characteristics non-invasively in the tumor lesions that can be used in conjunction with MRI is proton (^{1}H) MR Spectroscopy (MRS). Researchers have shown that ^{1}H MRS can be used to characterize breast cancers with improved diagnostic accuracy (22-26). Unfortunately, multi-voxel based novel MR spectroscopic imaging (MRSI) techniques using the speed advantage offered by echo-planar imaging (EPI) and improved spectral resolution offered by two-dimensional (2D) MR spectroscopy (MRS) have not been fully explored in breast cancer studies so far. Hence, a major task of this project is to combine echo-planar correlated spectroscopic imaging (EP-COSI) with DWI approach for improving the overall specificity of breast cancer detection.

Body:
i) __Proposed Task 1:__ To further optimize the multi-voxel based extension of the correlated spectroscopy (COSY) sequence, in which two spectral encodings will be combined with two spatial encodings. This four-dimensional (4D) data acquisition scheme will be accomplished utilizing the echo-planar imaging (EPI) approach that is commonly used for spatial encoding in MRI including DWI. (__Months 1-6__).

This task was completed already (September 2010-May 2011) as reported previously.

ii) __Proposed Task 2:__ To evaluate the EP-COSI data using a breast phantom containing two concentric spheres, the inner one containing several metabolites which have been reported in breast tissues surrounded by the outer phantom containing corn oil to mimic

*fatty tissues known to be in breast tissues, and to optimize the echo speed-factor and other acquisition parameters using the phantom (**Months 1-6**).*

This task was completed already (September 2010-August 2011) as reported in our 2012 report.

*iii) **Proposed Task 3:** To develop, evaluate and optimize the prior-knowledge basis set spectra using the GAMMA-simulation and breast phantom solutions as prior knowledge for the multi-voxel based COSY spectra recorded using the 3T MRI scanner (**Months 3-9**).*

Using the GAMMA library (27), a prior-knowledge basis-sets containing metabolites and lipids have been prepared as reported previously.

*iv) **Proposed Task 4:** To record the EP-COSI spectra in the fatty, glandular and ductal areas of healthy breasts. Twenty healthy female volunteers (25-70 years old) with no previous history of breast cancer will be investigated. (**Months 6-24**).*

Eleven healthy women (age=26-59 years) without any prehistory of breast cancer were investigated using the DWI and EP-COSI MRI protocol during the first two years as reported previously. Six more healthy women were investigated during the current year.

*v) **Proposed Task 5:** To record the multi-voxel-based 2D spectra in patients with benign and malignant breast cancer. The breast metabolite and lipid concentrations calculated from the multi-voxel data using the ProFit algorithm will be compared with LC-Model processed 1D spectral based MRSI data. Twenty patients with biopsy-proven breast cancer (ductal carcinoma and invasive lobular cancer), twenty patients with benign breast tumor (fibroadenoma, proliferative fibrocystic change and papillomas) will be investigated (**Months 6-24**).*

We had reported studying three women with benign (age=28-44 years) and 2 with malignant breast cancer (age=61 years) in our last annual report. In the current year, using a dedicated breast MRI coil, we have investigated four malignant and three benign cancer patients using the 4D EP-COSI sequence on the 3T MRI scanner.

Shown in Fig. 1 are the following: A) An axial MRI slice image recorded in a 38yo malignant breast cancer patient showing the EP-COSI localization (white box). B) an extracted COSY spectrum(2ml) recorded from the affected breast lesion and C) another extracted COSY spectrum(2ml) recorded from the unaffected breast fatty region. As reported previously (28), the 2D COSY spectrum from the suspicious mass showed elevated water and decreased lipid resonances.

Fig. 2 shows the following: A) An axial MRI slice image recorded in a 31yo benign breast cancer patient showing the EP-COSI localization. B) Multi-voxel EP-COSI spectra; C) and D) show 2ml COSY spectra recorded from the affected mass and a healthy region. These results are also in agreement with our earlier data on the SV-based L-COSY sequence (29-30).
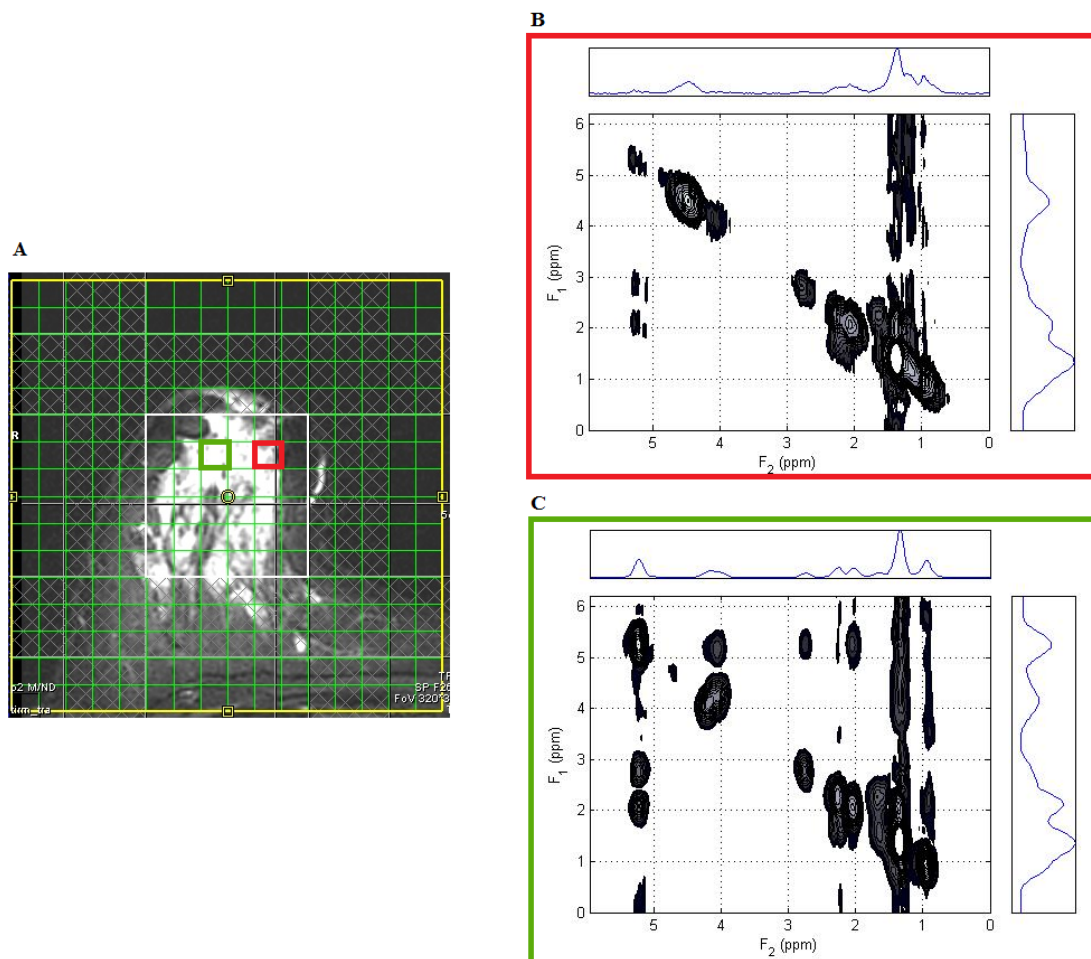
Figure 1. (A) An axial MRI slice image recorded in a 38 yo subject with malignant breast cancer showing the EP-COSI localization; the small white box shows the regions of interest (ROI) localized the EP-COSI sequence and the large white box with 16x16 grids shows the spatial localization encoded by the EP-COSI sequence. (B) A 2ml 2D COSY spectrum from the affected breast region. (C) A 2ml spectrum showing healthy fatty breast region.

Figure 2. (A) An axial MRI slice image recorded in a 31 yo subject with benign breast cancer (a hypo-intense mass) showing the EP-COSI localization; the small white box shows the regions of interest (ROI) localized the EP-COSI sequence and the large white box with 16x16 grids shows the spatial localization encoded by the EP-COSI sequence. (B) An extracted 2D COSY spectrum from the affected breast regions. (C) 2ml spectrum from the fatty breast region.
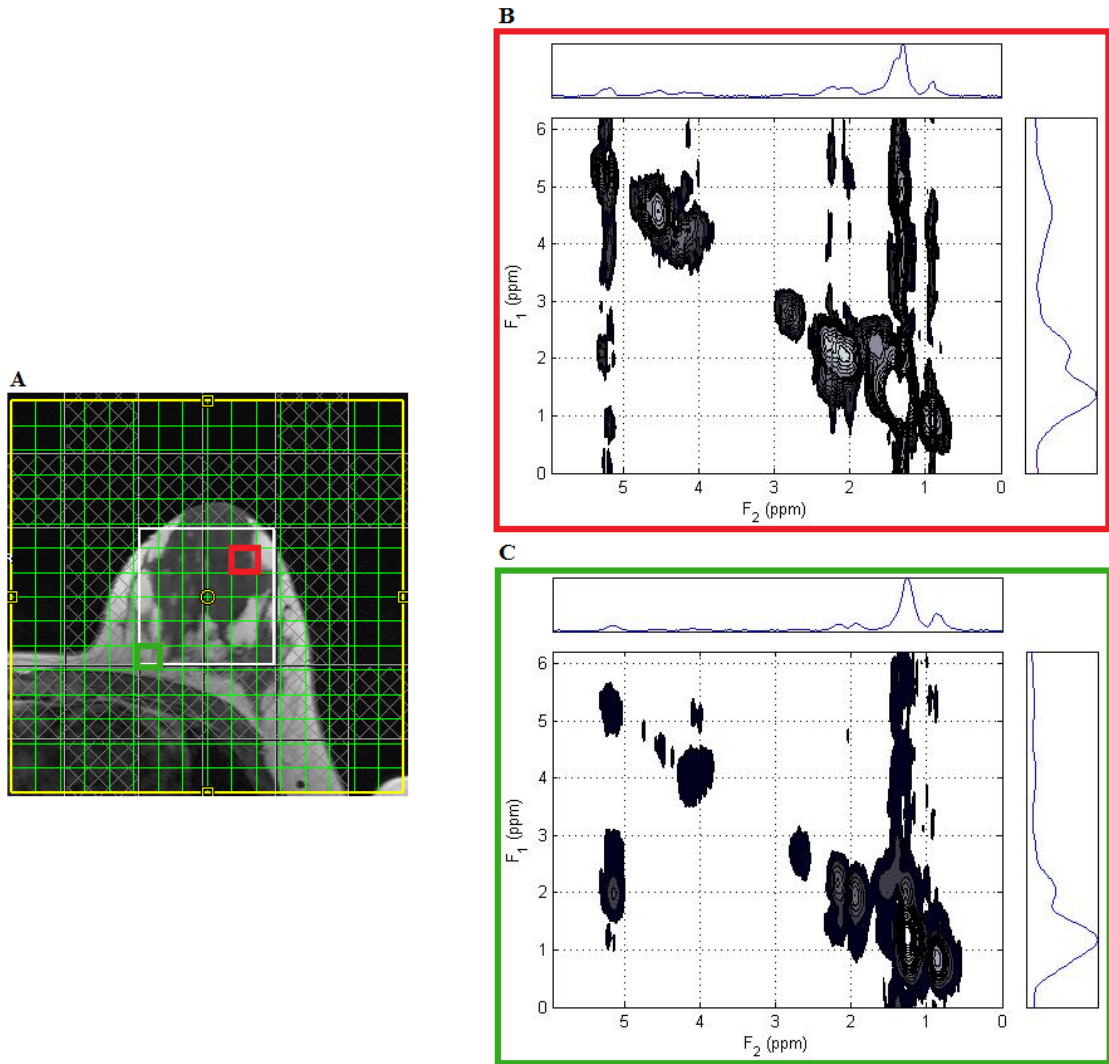
*vi) **Proposed Task 6:*** *To record multi-slice DWI in twenty patients with biopsy-proven breast cancer, twenty patients with benign breast tumor and twenty healthy women and to calculate the ADC maps. (**Months 6-24**).*

Figure 3. An axial ADC slice image recorded in the 38 yo subject with a malignant mass using the DWI sequence.
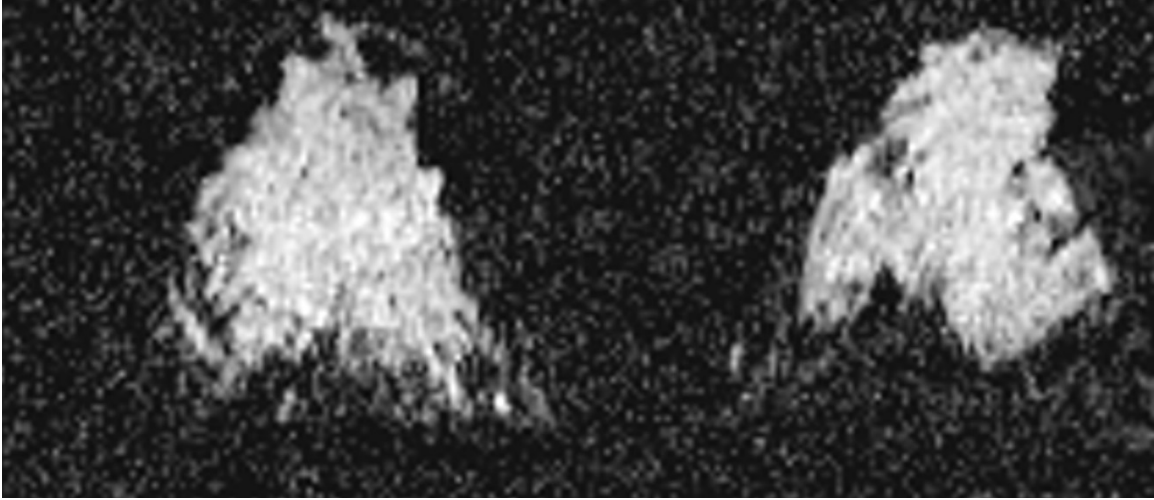
Figure 4. An axial ADC slice image recorded in the 31 yo subject with a benign mass in both breasts using the DWI sequence.
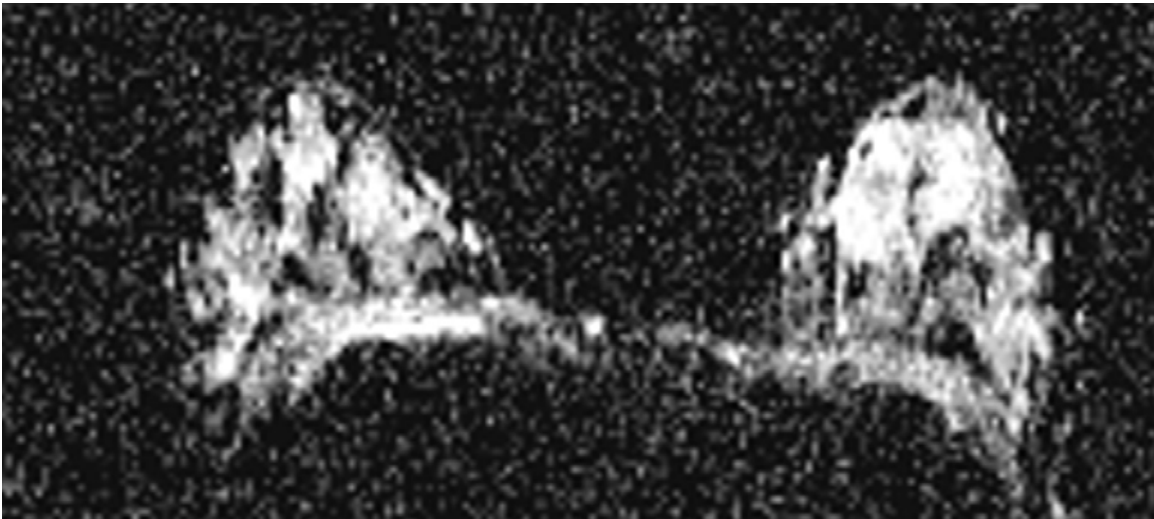
The diffusion weighted imaging (DWI) has been recorded in three women with benign and 4 with malignant breast cancer 3T MRI scanner using a dedicated breast MRI coil.

*vii) **Proposed Task 7:*** *To correlate the EP-COSI findings with that of DWI in differentiating benign from malignant breast cancers, and to calculate specificity, sensitivity and accuracy of the MRSI and DWI data in differentiating benign from malignant tumors. (**Months 6-24**).*

This task will be completed during the no-cost extension period.

Key Research Accomplishments

- The 4D EP-COSI has been successfully evaluated in 17 healthy women, 5 benign and 6 malignant breast cancer patients so far using the UCLA Radiology Siemens 3T MRI scanner equipped with a dedicated breast phased-array assembly. As summarized in the previous year reports, the 4D EP-COSI sequence is available at UCLA only as the sequence is not supplied by any of MRI manufacturers.
- The DWI-MRI protocol was successfully evaluated in a total of 17 healthy women, 5 benign and 6 malignant breast cancer patients so far.
- Our pilot results so far clearly demonstrate that the EP-COSI spectroscopic imaging sequence can be combined with a clinical breast DWI protocol with the total duration of less than an hour. The protocol is completely safe enough to be included in any MRI protocol to be evaluated in breast cancer for improving the overall specificity.
- Our recent work has focused on testing retrospective Maximum Entropy and Compressed Sensing of the 4D EP-COSI data so that the acquisition can be accelerated to less than 10 minutes which will lead to less imaging time for patients with breast cancer.

Reportable Outcomes:
A. Peer-reviewed Publications: 1) Burns B, Wilson N, Furuyama JK and Thomas MA. Non-uniformly under-sampled multi-dimensional spectroscopic imaging in vivo: maximum entropy versus compressed sensing reconstruction. NMR Biomed 2014;27: 191-201.
2) Burns B, Wilson N and Thomas MA. Split-Bregman-based Group-Sparse Reconstruction of multi-dimensional MR Spectroscopic Imaging data. ISBI Beijing, 2014 (in press)

B. Presentations: We report one conference presentation as shown below.
- An oral presentation at the ISBI conference, Beijing. *China,* April28-May 2, 2014 (to be presented)

C. Books: None on Breast Cancer Research based.

Conclusions: So far, the MR scanning protocol including EP-COSI and DWI-MRI has been evaluated in 17 healthy women, 5 benign and 6 malignant breast cancer. We will continue to recruit 8-10 malignant, 4-6 benign and 3 healthy women during the next year. The UCLA mammo co-investigators, namely Dr. Naneltte DeBruhl and Dr.

Lawrence Bassett have promised us to help recruiting more patients in the current no-cost extension year.

References

1. Biersack B, Schobert R. Indole Compounds against Breast Cancer: Recent Developments. Curr Drug Targets. 2012 Nov 6. [Epub ahead of print].
2. Ries LAD, Eisner MP, Kosary CL, Hankey BF, Miller BA, Clegg L, Mariotto A, Feuer EJ, Edwards BK (eds). SEER Cancer Statistics Review 1975-2002. National Cancer Institute: Bethesda, MD. http://seer.cancer.gov/csr/1975-2002/, based on November 2004 SEER data submission, posted online 2005.
3. Sabel M and Aichinger H. Recent developments in breast imaging. Phys Med Biol 1996; 41 (3): 315-68.
4. Morris EA. Diagnostic Breast MR Imaging: Current Status and Future Directions. Radiol Clin N America 2007; 45: 863-880.
5. Lehman CD, Isaacs C, Schnall MD, Pisano ED, Ascher SM, Weatherall PT, Bluemke DA, Bowen DJ, Marcom PK, Armstrong DK, Domchek SM, Tomlinson G,Skates SJ, Gatsonis C. Cancer Yield of mammography, MR and US in high-risk women: Perspective multi-institution breast cancer screening study. Radiology. 2007; 244: 381-388.
6. Saslow D, Boetes C, Burke W, Harms S, Leach MO, Lehman CD, Morris E, Pisano E, Schnall M, Sener S, Smith RA, Warner E, Yaffe M, Andrews KS, Russell CA. American Cancer Society Guidelines for Breast Screening with MRI as an Adjunct to Mammography. CA Cancer J Clin. 2007; 57: 75-89.
7. Weinreb JC and Newstead G. MR imaging of the breast, Radiology 1995; 196(3): 593-610.
8. Harms SE and Flamig DP. MR imaging of the breast. J Magnetic Resonance Imaging 1993; 2:277-83.
9. Graham SJ, Bronskill MJ, et al. Quantitative correlation of breast tissue parameters using magnetic resonance and X-ray mammography. British Journal Cancer 1996; 73(2): 162-8.
10. Stelling CB. MR imaging of the breast for cancer evaluation. Current status and future directions. Radiologic Clinics of North America 1995; 33(6):1187-204.
11. Cohen EK, Leonhardt CM, Shumak RS, Soutar IC, Bukhanov K, Fishell EK, Plewes DB. Magnetic resonance imaging in potential post surgical recurrence of breast cancer: pitfalls and limitations. Canadian Association of Radiologists Journal 1996; 47(3):171-6.
12. Hickman PF, Moore NR and Shepstone BJ. The indeterminate breast mass: assessment-using contrast enhanced magnetic resonance imaging. Brit J Radiology 1994; 67(793):14-20.
13. Kerslake RW, Fox JN, Carleton PJ, Imrie MJ, Cook AM, Bowsley SJ, Horsman A. A dynamic contrast-enhanced and fat suppressed magnetic resonance imaging in suspected recurrent carcinoma of the breast: preliminary experience. Brit J Radiology 1994; 67(804): 1158-68.
14. Kvistad KA, Rydland J, Vainio J, Smethurst HB, Lundgren S, Fjøsne HE, Haraldseth O. Breast Lesions: evaluation with dynamic contract-enhanced T1 weighted MR Imaging and with T2* weighted first-pass perfusion MR imaging. Radiology 2000; 216: 545-553.
15. Furman-Haran E, Grobgeld D, Kelcz F, Degani H.. Critical role of spatial resolution in dynamic contrast-enhanced breast MRI. J Magn Reson Imag 2001; 13: 862-867.
16. Liu PF, Debatin JF, Caduff RF, Kacl G, Garzoli E, Krestin GP. Improved diagnostic accuracy in dynamic contrast-enhanced MRI of the breast by combined quantitative and qualitative analysis. Brit J Rad 1998; 71:501-509.

17. Le Bihan D, Breton E, Lallemand D, renier P, Cabanis E, Laval-Jeantet M. MR imaging of intravoxel incoherent motions: application to diffusion and perfusion in neurologic disorders. Radiology 1986;161:401–407.

18. Bammer. Basic principles of diffusion-weighted imaging. European journal of radiology. 2003 Mar;45(3):169-84.

19. Belli P, Constantini M, Bufi E, Magistrelli A, La Torre G, Bonomo L. Diffusion weighted imaging in breast lesion evaluation. Radiol Med 2009.

20. Sharma U, Danishad KK, Seenu V, Jagannathan NR. Longitudinal study of the assessment by MRI and diffusion-weighted imaging of tumor response in patients with locally advanced breast cancer undergoing neoadjuvant chemotherapy. NMR Biomed 2009;22:104–113.

21. Bogner W, Gruber S, Pinker K, Grabner G, Stadlbauer A, Weber M, Moser E, Helbich TH, Trattnig S. Diffusion-weighted MR for Differentiation of Breast Lesions at 3.0 T: How Does Selection of Diffusion Protocols Affect Diagnosis? Radiology 2009;253:341-351

22. Gribbestad IS, Sitter B, Lundgren S, Krane J, Axelson D. Metabolite composition in breast tumors examined by proton nuclear magnetic resonance spectroscopy. Anticancer Res 1999; 19: 1737-1746.

23. Aboagye EO, Bhujwalla ZM. Malignant transformation alters epithelial cells. Cancer Res 1999; 59(1): 80-84.

24. Mountford CE, Somorjai RL, Malycha P, Gluch L, Lean C, Russell P, Barraclough B, Gillett D, Himmelreich U, Dolenko B, Nikulin AE, Smith IC. Diagnosis and prognosis of breast cancer by magnetic resonance sprectroscopy of fine-needle aspirates analyzed using a statistical classification strategy. BR J Surg 2001; 88: 1234-1240.

25. Stanwell P, Glutch L, Clark D, Tomanek B, Baker L, Giuffrè B, Lean C, Malycha P, Mountford C. Specificity of choline metabolites for in vivo diagnosis of breast cancer using 1H MRS at 1.5T. Eur. Radiology 2005; 50: 1134-1143.

26.Roebuck JR, Cecil KM, Schnall MD, Lenkinski RE. Human breast lesions: characterization with proton MR spectroscopy. Radiology 1998; 209: 269-275.

27. Smith SA, Levante TO, Meier BH and Ernst RR. Computer Simulations in Magnetic Resonance. An object oriented programming approach. J Magn Reson 1994; A106: 75-105.

28. Lipnick S, Verma G, Ramadan S, Furuyama J and Thomas MA. Echo-Planar based Correlated Spectroscopic Imaging (EP-COSI): Implementation and Pilot Evaluation in Human Calf Muscle. Magn Reson Med 2010;64(4):947-956.

29. Thomas MA, Binesh N, Yue K and DeBruhl N. Volume-Localized Two-Dimensional Correlated Magnetic Resonance Spectroscopy of Human Breast Cancer. J Magn Reson Imaging 2001;14:181-186.30. Lipnick S, Liu X, Sayre J, Bassett L, DeBruhl N and Thomas MA. Combined DCE-MRI and single-voxel 2D MRS for differentiation between benign and malignant breast lesions. NMR Biomed 2010; 23: 922–930.

Appendix:

A) A copy of our manuscript published in 2014 issue of NMR in Biomedicine
B) A preprint of our manuscript currently in press: Burns B, Wilson N and Thomas MA. Split-Bregman-based Group-Sparse Reconstruction of multi-dimensional MR Spectroscopic Imaging data. ISBI2014 (in press).

Non-uniformly under-sampled multi-dimensional spectroscopic imaging *in vivo*: maximum entropy *versus* compressed sensing reconstruction

Brian Burns[a,b], Neil E. Wilson[a,c], Jon K. Furuyama[a,c] and M. Albert Thomas[a,b,c]*

The four-dimensional (4D) echo-planar correlated spectroscopic imaging (EP-COSI) sequence allows for the simultaneous acquisition of two spatial (k_y, k_x) and two spectral (t_2, t_1) dimensions *in vivo* in a single recording. However, its scan time is directly proportional to the number of increments in the k_y and t_1 dimensions, and a single scan can take 20–40 min using typical parameters, which is too long to be used for a routine clinical protocol. The present work describes efforts to accelerate EP-COSI data acquisition by application of non-uniform under-sampling (NUS) to the k_y–t_1 plane of simulated and *in vivo* EP-COSI datasets then reconstructing missing samples using maximum entropy (MaxEnt) and compressed sensing (CS). Both reconstruction problems were solved using the Cambridge algorithm, which offers many workflow improvements over other l_1-*norm* solvers. Reconstructions of retrospectively under-sampled simulated data demonstrate that the MaxEnt and CS reconstructions successfully restore data fidelity at signal-to-noise ratios (SNRs) from 4 to 20 and 5× to 1.25× NUS. Retrospectively and prospectively 4× under-sampled 4D EP-COSI *in vivo* datasets show that both reconstruction methods successfully remove NUS artifacts; however, MaxEnt provides reconstructions equal to or better than CS. Our results show that NUS combined with iterative reconstruction can reduce 4D EP-COSI scan times by 75% to a clinically viable 5 min *in vivo*, with MaxEnt being the preferred method. Copyright © 2013 John Wiley & Sons, Ltd.

Keywords: EP-COSI; maximum entropy; compressed sensing; non-uniform under-sampling; spectroscopy; spectroscopic imaging

INTRODUCTION

Changes in metabolite concentrations as a result of the altered metabolism of cancer can be detected non-invasively using one-dimensional (1D) MRS *in vivo* (1–3). However, the overlap of spectral peaks in 1D MRS is a major impediment to the identification of individual metabolites. Two-dimensional (2D) MRS has increased spectral dispersion over 1D MRS and can disentangle overlapping complex spectral peaks (4). Single-voxel 2D MRS has been shown to increase the specificity and sensitivity of tumor grade classification when used with dynamic contrast-enhanced MRI in the breast (5). However, the acquisition of multiple t_1 increments per voxel to form the second spectral dimension limits its ability to provide multi-voxel coverage because of the long scan times needed to combine two spectral and two spatial dimensions.

With the advent of echo-planar spectroscopic imaging (EPSI), MRSI scans with one spectral and two spatial dimensions can be completed within clinically acceptable times by interleaving the acquisition of a spatial and spectral dimension within the EPSI readout (6–8). The four-dimensional (4D) echo-planar correlated spectroscopic imaging (EP-COSI) (9) sequence allows the acquisition of two spatial (k_y, k_x) and two spectral (t_2, t_1) dimensions in a single recording to form 4D MRSI. The sequence interleaves the acquisition of the k_x and t_2 dimensions within the EPSI readout, but k_y and t_1 are incrementally acquired as indirect dimensions during each TR. The EP-COSI sequence has the benefits of increased spectral dispersion and multi-voxel support, which improves metabolite identification over multiple spatial

regions simultaneously; however, its scan time is directly proportional to the number of increments in the k_y and t_1 dimensions. An EP-COSI scan using typical parameters of TR/TE = 1.5 s/30 ms and k_y/t_1 = 16/100 can take 40 min, which is too long to be used within a routine clinical protocol.

---

* Correspondence to: M. Albert Thomas, Radiological Sciences, David Geffen School of Medicine at UCLA, 10833 Le Conte Avenue, Los Angeles, CA 90095–1721, USA. E-mail: athomas@mednet.ucla.edu

a B. Burns, N. E. Wilson, J. K. Furuyama, M. A. Thomas
  Department of Radiological Sciences, David Geffen School of Medicine, University of California, Los Angeles, CA, USA

b B. Burns, M. A. Thomas
  Department of Biomedical Engineering, University of California, Los Angeles, CA, USA

c N. E. Wilson, J. K. Furuyama, M. A. Thomas
  Biomedical Physics IDP, University of California, Los Angeles, CA, USA

Abbreviations used: *1D/2D/3D/4D, one-/two-/three-/four-dimensional; Asp, aspartate; COSY, correlated spectroscopy; Cr, creatine; CS, compressed sensing; EP-COSI, echo-planar correlated spectroscopic imaging; EP-JRESI, echo-planar J-resolved spectroscopic imaging; EPSI, echo-planar spectroscopic imaging; FFT, fast Fourier transform; FMETD, methyl fat; FWHM, full width at half-maximum; Glx, glutamate and glutamine; MaxEnt, maximum entropy; NUS, non-uniform under-sampling/under-sampled; PSF, point spread function; RMSE, root-mean-square error; SNR, signal-to-noise ratio; tCho, total choline (choline + glycerophosphocholine + phosphocholine); TGFR, triglyceryl fat; UFD, olefinic fat; UFL, unsaturated fatty acid left; UFR, unsaturated fatty acid right.*

When the Fast Fourier Transform (FFT) is used to transform uniformly sampled 4D MRSI data (k_y, k_x, t_2, t_1) to the spatial, spectral domain (Y, X, F_2, F_1), decreasing scan times require a reduction in either the k_y spatial or t_1 spectral dimension through truncation or lower sampling rates, and a corresponding unwanted reduction in resolution or bandwidth. However, non-uniform under-sampling (NUS) of the spatial, spectral k_y–t_1 plane, in combination with iterative non-linear reconstruction, can be used to accelerate the collection of 4D MRSI data *in vivo*, whilst preserving the spatial and spectral resolutions and bandwidths (10).

Earlier work has demonstrated the feasibility of under-sampling the mixed-domain k_y–t_1 plane of a 4D echo-planar *J*-resolved spectroscopic imaging (EP-JRESI) dataset and reconstructing the missing points with compressed sensing (CS) (10), a popular method of non-linear iterative image reconstruction which promotes data sparsity in the reconstruction domain and data fidelity in the sample domain (11,12). The nature of spatial, spectral NUS artifacts in the k_y–t_1 plane was explored, and it was shown that l_1-*norm*-based CS reconstruction is a viable means of reducing the scan times of 4D EP-JRESI *in vivo* through NUS. In recent years, CS reconstruction has been successfully applied to NUS MRI (13,14), three-dimensional (3D) MRSI (15), dynamic MRI (16,17), and multi-dimensional Nuclear Magnetic Resonance (NMR) (23).

Maximum entropy (MaxEnt) image reconstruction is an alternative non-linear iterative reconstruction technique to CS. Rather than minimizing transform sparsity, it maximizes the entropy of the data in the reconstruction domain, whilst preserving data fidelity in the sample domain (18,19). MaxEnt has been successfully used to reconstruct under-sampled images in astronomy and multi-dimensional spectra in NMR (19–21). However, MaxEnt has not been applied to the mixed-domain k_y–t_1 plane of a 4D MRSI dataset *in vivo*.

The use of entropy as a regularizer in image reconstruction predates l_1-*norm*-based CS reconstruction and continues to be used extensively in the reconstruction of under-sampled NMR spectra in spite of the popularity of CS in other fields. It was first suggested by Frieden (18) in the early 1970s after Jaynes (22) proposed the idea of the Principle of Maximum Entropy, which describes the MaxEnt distribution as the 'maximally non-committal distribution with regard to unavailable data'. This principle presents the MaxEnt prior as one that assumes nothing about the unavailable data; by assuming nothing about those points, their possible values are all equally likely to occur, and the reconstruction is that which most closely conforms to the uniform distribution, i.e. is flat. Peaks in the reconstruction domain are the result of signals from the sampled data, and any artifacts from the missing data points are removed because they represent states of low entropy that are not the result of k-space or time-domain signals.

In this article, we compare the MaxEnt and l_1-*norm*-based CS reconstructions of NUS 4D EP-COSI data and show that MaxEnt is a viable alternative to CS for reducing scan times 4× in human breast *in vivo*. We quantitatively characterize the MaxEnt and CS reconstructions by comparing results for retrospectively NUS-simulated 4D EP-COSI data at varying levels of signal-to-noise ratio (SNR) and NUS rates. We show that retrospectively 4× NUS 4D EP-COSI *in vivo* breast data reconstructed using either MaxEnt or CS show a comparable spatial, spectral resolution to the fully sampled data. In addition, we show that MaxEnt and CS reconstructions of prospective 4× NUS 4D EP-COSI scans from the same breast study as the retrospective data, using the same mask and sequence parameters, compare favorably with the retrospective and fully sampled data.

Throughout this article, the NUS dataset that has not been reconstructed and has zeros in place of missing samples is referred to as the zero-augmented dataset to distinguish it from the MaxEnt and CS reconstructions.

EXPERIMENTAL DETAILS

4D MaxEnt and CS reconstruction: theory

MaxEnt and l_1-*norm*-based CS were used to reconstruct the NUS k_y–t_1 plane of the 4D EP-COSI datasets.

l_1-*norm*-based CS image reconstruction of 4D MRSI data is formulated as a constrained convex optimization problem (10–12):

$$\text{minimize } \|\psi m\|_1 \quad s.t \ \|K\mathcal{F}m - d\|_2^2 \leq C_0 \quad \text{[1]}$$

where $m = (y, x, F_2, F_1)$ is the reconstructed spatial, spectral-domain data, $\mathcal{F}$ is the 4D Fourier operator, K is the NUS mask that determines which samples were acquired in the k_y–t_1 plane, $d = (k_y, k_x, t_2, t_1)$ is the k-space, time-domain sampled data, C_0 is the standard deviation of the noise in d and ψ is a known sparse transform. ψ was chosen to be the identity transform because m was already self sparse as shown in ref. (10).

MaxEnt image reconstruction of 4D MRSI data solves a similar problem to CS, but uses $S_{1/2}$ entropy instead of the l_1-*norm* (19–21):

$$\text{maximize } S(m)_{1/2} \quad s.t \ \|K\mathcal{F}m - d\|_2^2 \leq C_0 \quad \text{[2]}$$

where $S(m)_{1/2}$ is the entropy of the estimated spectrum, and the remaining terms are identical to those in the CS problem. $S_{1/2}$ entropy is a concave function with a global maximum and no local extrema, and so there is a single solution that satisfies the problem within the feasible set of solutions defined by the data fidelity constraint as shown in Fig. 1 (24). As can be seen, $S_{1/2}$ entropy has a global extremum and has slightly more curvature than the l_1-*norm*, but has far less curvature than the l_2-*norm*.

The entropy used in the MaxEnt reconstruction was not the often used $-\sum p\log(p)$ entropy introduced by Shannon (25), but the $S_{1/2}$ entropy derived by Daniell and Hore (20) specifically
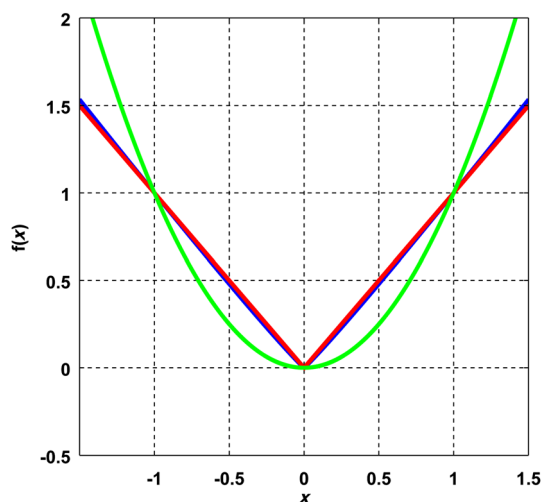

Figure 1. Plot showing $-S_{1/2}$ entropy (blue), l_1-*norm* (red) and l_2-*norm* (green). Each function has been normalized to equal unity at $|x| = 1$.

for NMR spectra originating from spin $^1/_2$ nuclei, such as ^{1}H, used in MRSI:

$$S(m)_{\frac{1}{2}} = -\sum_{i=1}^{i=N} \frac{|m_i|}{def} \log\left(\frac{|m_i|/_{def} + \sqrt{4 + (|m_i|/_{def})}}{2}\right)$$
$$- \sqrt{4 + \left(\frac{|m_i|}{def}\right)^2} \qquad [3]$$

where *def* is a scaling parameter related to the sensitivity of the scanner and is calculated for m of length N as $\sqrt{C_0/_N}$ (21). $S_{1/2}$ is used because the underlying physical processes that produce an MR spectrum are not based on discrete particle events and so cannot be modeled by simple Poisson-distributed processes as required for the derivation of Shannon entropy (26). They are governed by the density matrix of the spin system under investigation, and so the statistical distribution is different. Equation [3] was derived from first principles using both a classical spin model and a quantum mechanical model. Neither model made any assumptions on the initial state of the spin system nor the pulse sequence used. This equation can be applied to any MR spectrum originating from spin $^1/_2$ nuclei, and addresses previous concerns regarding the use of entropy in MRS and MRI reconstruction (27).

In order to remove any differences between the MaxEnt and CS reconstructions caused by differences in the solvers used, both problems were solved by a Matlab implementation of the Cambridge algorithm (19). This recasts the image reconstruction problem into an unconstrained convex optimization problem and uses a variant of the conjugate gradient method to iteratively find the extrema in two phases; the first phase minimizes the fidelity constraint and the second phase minimizes or maximizes the objective function, while keeping the fidelity constraint minimized. The stopping criterion for the problem is reached when the gradients of the objective $O(m)$ and the fidelity constraint $C(m)$ are parallel: $\left|\frac{\nabla O}{\|\nabla O\|_2} - \frac{\nabla C}{\|\nabla C\|_2}\right| < 0.001$. Specific details on the algorithm and modifications to accommodate multi-dimensional MR data can be found in ref. (21).

The Cambridge algorithm calculates the gradient $\nabla\|m\|_1 \in \mathbb{C}^N$ and Hessian $\nabla^2\|m\|_1 \in \mathbb{C}^{2Nx2N}$ of the objective function, which are not defined for $\|m\|_1$ when $m_i = 0$. Therefore, in order to solve the l_1-*norm*-based CS reconstruction problem, $\|m\|_1$ was redefined as:

$$\|m\|_1 = \sum_{i=1}^{i=N} \sqrt{\mathcal{R}(m_i)^2 + \mathfrak{I}(m_i)^2 + \epsilon} \qquad [4]$$

where $\mathcal{R}$ and $\mathfrak{I}$ were the real and imaginary components of m_i, and ϵ is a small non-zero value to prevent $m_i = 0$. The gradient and Hessian were then defined as:

$$\nabla\|m\|_1 = W^{-1}m \qquad [5]$$

$$\nabla^2\|m\|_1 = \begin{bmatrix} |m_i|^{-1}(1 - \mathcal{R}(m_i))|m_i|^{-2} & -\mathfrak{I}(m_i)\mathcal{R}(m_i)|m_i|^{-3} \\ -\mathfrak{I}(m_i)\mathcal{R}(m_i)|m_i|^{-3} & |m_i|^{-1}(1 - \mathfrak{I}(m_i))|m_i|^{-2} \end{bmatrix} \qquad [6]$$
$$= 2 \times 2 \text{ block diagonal matrix}$$

where $W \in \mathbb{C}^{NxN}$ is a diagonal matrix with $w_{ii} = |m_i|$, and element m_i is associated with the ith 2×2 block in the Hessian. The gradient and Hessian of $S(m_i)_{\frac{1}{2}}$ are defined in ref. (21). Only the 2×2 diagonal blocks of the $\|m\|_1$ and $S(m_i)_{\frac{1}{2}}$ Hessians were stored in memory during reconstruction, not the full matrices.

Sample mask generation

The k_y–t_1 plane of the 4D EP-COSI datasets used in these experiments was under-sampled using 2D Poisson-gap sample masks that were generated using a modified 1D Poisson-gap process (28). In 1D Poisson-gap sample masks, the gaps between samples follow a Poisson distribution, whereas the 2D extension follows the convention that gaps between spaces follow a Poisson distribution. However, both conventions result in the spaces and sample points following Poisson distributions. Poisson-distributed masks avoid large gaps between samples, which are detrimental to the reconstruction, while ensuring that the samples are randomly distributed (29). Compared with other distributions, Poisson-distributed masks create the fewest aliasing artifacts in the Fourier domain and preserve the SNR of the under-sampled data (30).

The effects of the sample mask on the peak amplitude and lineshape of spectral reconstructions are well documented (29,31,32). Sample mask densities that follow the time-domain NMR signal envelope and sample more points at higher SNR have spectral reconstructions with lower root-mean-square errors (RMSEs) and less non-linearity compared with sample masks that do not. The t_1 dimensions of the EP-COSI datasets in this work were apodized with a sine-squared filter to enhance the cross-peaks (9), but, because of T_2^* decay, the filtered EP-COSI data had a skewed sine-squared signal envelope; therefore, the 2D Poisson-gap sample mask density was modulated along t_1 with a skewed sine-squared function (33). The k_y dimension was modulated by an exponential decay function similar to that used previously to maximize spatial SNR (34).

The sample density of a Poisson-gap mask can be modulated by the rate parameter λ which determines both the mean and variance of a Poisson distribution. The probability of generating a gap g from a Poisson distribution is characterized by:

$$p(g, \lambda) = (\lambda^g \cdot e^{-\lambda})/g! \qquad [7]$$

For large λ, large values of g are more likely, and for small λ, small values of g are more likely. Therefore, the probability of g can be modulated by varying the value of λ according to a sine or exponential decay function, and the probability of large gaps between spaces can be increased where the SNR is highest in the MR signal envelope (28). To generate g as a function of λ, a Poisson process can be simulated using various techniques that do not depend on an *a priori* knowledge of g as above (35). For these experiments, the *poissrnd(λ)* function in Matlab was used to generate g as a function of λ. It takes as input an array of λ and returns an array of gaps with local mean and variance λ.

2D Poisson-gap sample masks were iteratively generated in Matlab by combining the 1D distributions of t_1 and k_y until the desired NUS rate was reached.

Examples of the 2D λ, gap and mask arrays generated by 2D Poisson-gap are shown in Fig. 2; as the size of λ and the spacing gaps increase, the sample density increases in that area of the mask. The magnitude point spread function (PSF) of the mask is shown and demonstrates the viability of this approach; the single dominant central peak with small side-lobes, surrounded by low-amplitude, incoherent artifacts, is the desired profile of
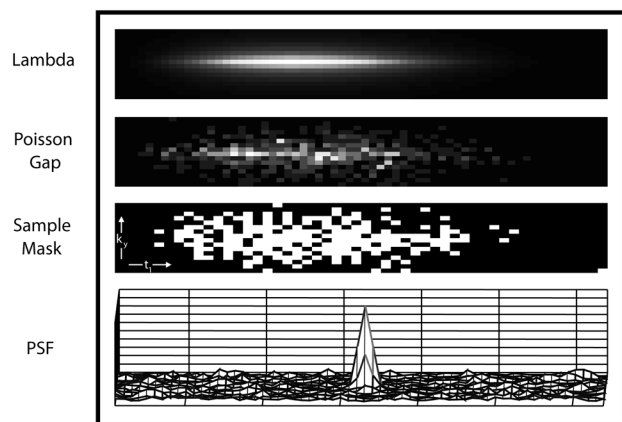
Figure 2. Poisson sample mask creation along the k_y–t_1 plane for echo-planar correlated spectroscopic imaging (EP-COSI). Top: modulated values of λ. Upper middle: Poisson-distributed values for each λ indicating the gap between spaces in the sample distribution. Lower middle: resulting two-dimensional (2D) Poisson-gap sample mask. Bottom: magnitude point spread function (PSF) of the 2D sample mask.

a NUS mask PSF (36,37). Incoherent sampling artifacts will have low amplitudes and spurious peaks caused by coherent aliasing will be negligible.

MR simulations

The effects of SNR and under-sampling rate on the reconstructions were quantitatively assessed using a noise-free simulated 4D EP-COSI dataset that contained choline + glycerophosphocholine + phosphocholine (total choline, tCho), glutamate + glutamine (Glx), creatine (Cr), aspartate (Asp) or nothing in each voxel, as represented in the top of Fig. 3 by a diagonal peak from each metabolite. Each metabolite was simulated using the GAMMA NMR libraries (38) from a 3T localized 2D correlated spectroscopy sequence (39) with the following parameters: 100 t_1 increments, 1024 points in t_2, TR/TE = 1.5 s/30 ms, and spectral bandwidths of 1250 and 2000 Hz along F_1 and F_2, respectively. Each 2D spectrum was line broadened by 10 Hz and apodized by a sine-squared filter along t_1 and a skewed sine-squared filter with skew parameter 0.5 along t_2. No baseline corrections were performed on the spectra.

They were then copied into an 8×8 spatial grid to simulate spatially distributed metabolites as follows: the upper left quadrant contained 2×2 voxels of tCho, the upper right quadrant contained 2×2 voxels of Cr, the lower left quadrant contained 2×2 voxels of Glx and the lower right quadrant contained 2×2 voxels of Asp.

As a result of under-sampling the k_y–t_1 plane, the spatial, spectral artifacts caused the tCho and Glx voxels to alias into each other and the Cr and Asp voxels to alias into each other, as illustrated by the zero-augmented data at the bottom of Fig. 3. This changed the integrated peak area contained within each metabolite as the spatial, spectral separation between the metabolites broke down.

Noise was added to the simulated noise-free 4D EP-COSI dataset to model the SNRs of 2–20 in increments of 2. It was under-sampled 5×, 2.5×, 1.67× and 1.25×, and then separately reconstructed by MaxEnt and CS. The SNR was varied by simulating different levels of thermal noise in the dataset by adding univariate Gaussian noise to the noise-free real and imaginary channels of the 4D EP-COSI dataset (40). The desired SNR was achieved by ensuring that the additive noise signal power (σ^2) was equal to 1/SNR of the noise-free dataset signal power (ω^2), such that:

$$\text{noisy data} = \text{noise free data} + \frac{\omega^2}{\sigma^2 \times \text{SNR}} \times \text{noise} \qquad [8]$$

Because the additive noise was random, each SNR was simulated and reconstructed 20 times per sample mask to account for random fluctuations in the reconstruction. The sampling masks were created using the 2D Poisson-gap method described earlier.

MRSI

The breasts of three healthy volunteers were scanned using the 4D EP-COSI sequence on a Siemens (Siemens AG, Erlangen, Germany) 3T Trio scanner with the following parameters: voxel size, $1 \times 1 \times 1$ cm^3, 50 t_1 increments, TR/TE/averages = 1.5 s/30 ms/1, field of view, 16×16 cm^2 FOV, and spectral bandwidths of 1250 Hz and 1190 Hz along F_1 and F_2, respectively. Each breast was scanned twice: a 4× prospective NUS scan and a fully sampled scan using the same field of view and shim. The NUS scan took 5 min to complete and the

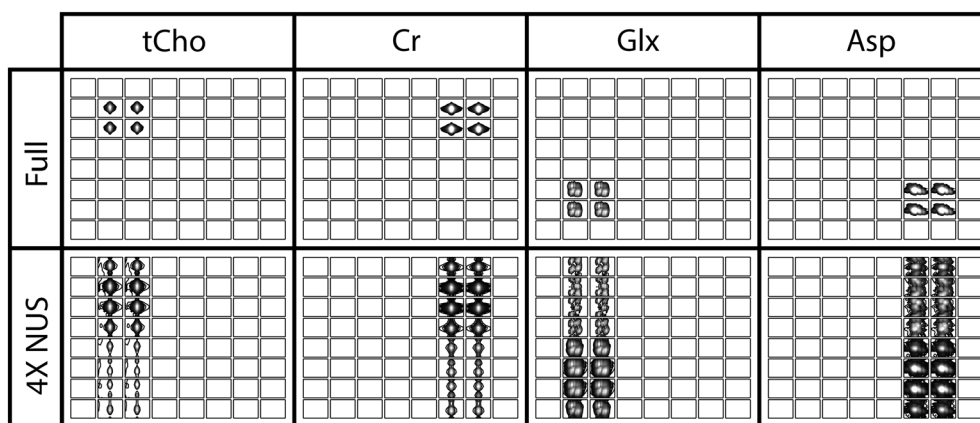
Figure 3. Simulated quad phantom illustration. Top: spatial distribution of tCho [total choline (choline + glycerophosphocholine + phosphocholine)], Cr (creatine), Glx (glutamate and glutamine) and Asp (aspartate) diagonal peaks when fully sampled. Bottom: spatial distribution of the same tCho, Cr, Glx and Asp diagonal peaks of the 4× non-uniform under-sampled (NUS) zero-augmented dataset.

fully sampled scan took 20 min. Both scans were first apodized using a sine-squared filter along t_1 and a skewed sine-squared filter with skew parameter 0.5 along t_2. No baseline corrections were performed on the *in vivo* breast data. The fully sampled scans were then retrospectively under-sampled 4× using the same mask as employed in the prospective scan shown in Fig. 4, and both NUS datasets were then reconstructed using MaxEnt and CS.

RESULTS

MR simulations

Quantitative results for the MaxEnt and CS reconstructions of the simulated 4D EP-COSI dataset at different NUS rates and SNRs are shown in Fig. 5. The top panel shows the mean RMSE *versus* SNR for zero-augmented and reconstructed datasets at each NUS rate. The RMSE provides an estimate of the reconstruction

Figure 4. Non-uniform under-sampling (NUS) mask used to under-sample the k_y–t_1 plane 4× in Figs 8 and 9.
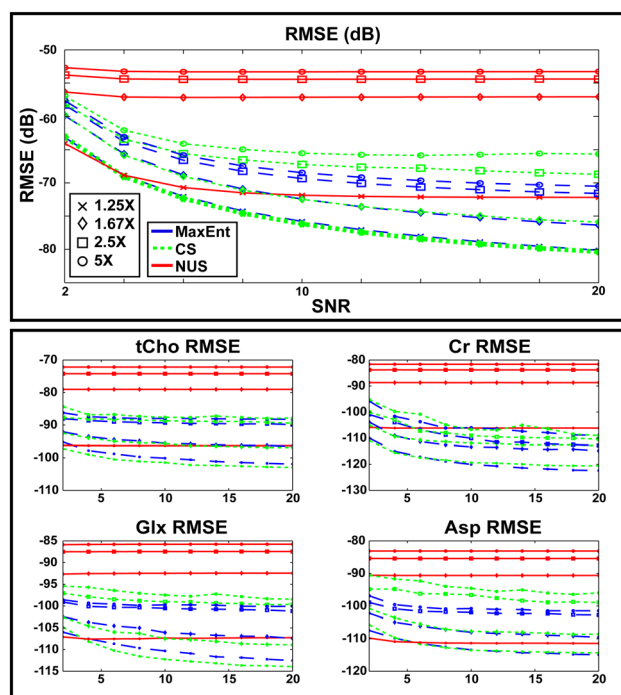

Figure 5. Metrics comparing the zero-augmented, maximum entropy (MaxEnt)-reconstructed and compressed sensing (CS)-reconstructed four-dimensional (4D) echo-planar correlated spectroscopic imaging (EP-COSI) simulated data. Top: overall root-mean-square errors (RMSEs) of each dataset *versus* signal-to-noise ratio (SNR) for 5×, 2.5×, 1.67× and 1.25× non-uniform under-sampling (NUS) rates. Bottom: tCho [total choline (choline + glycerophosphocholine + phosphocholine)], Cr (creatine), Glx (glutamate and glutamine) and Asp (aspartate) metabolite-specific RMSEs for each dataset *versus* SNR for 5×, 2.5×, 1.67× and 1.25× NUS rates.

accuracy with respect to a fully sampled reference dataset that increases as the two datasets become more dissimilar. The RMSE was calculated in the spatial, spectral domain as:

$$\text{RMSE} = \frac{1}{N}\sqrt{\Sigma(|\text{data}| - |\text{full}|)^2} \qquad [9]$$

where N is the number of data points, 'full' is the fully sampled dataset and 'data' is the zero-augmented or reconstructed dataset. Error bars are not shown because the standard deviations were three to four orders of magnitude smaller than the mean RMSEs and did not vary noticeably over the NUS rate or SNR. As can be seen, the RMSE of the zero-augmented dataset increases as the NUS rate increases, but does not vary considerably with SNR, except at low NUS rates. Both the CS and MaxEnt reconstructions show large decreases in RMSE at each SNR and NUS rate, but, at low SNRs, RMSE begins to rise. At low NUS rates, CS and MaxEnt have comparable RMSEs at each SNR; however, at higher NUS rates, the RMSEs for the MaxEnt reconstruction are lower than for CS, and this difference increases with SNR.

The bottom panel of Fig. 5 shows the average RMSE of the diagonal and cross-peaks of tCho, Glx, Cr and Asp *versus* SNR of the zero-augmented and reconstructed datasets. The RMSEs were calculated over the metabolite peaks at the ppm locations listed in Table 1. Each RMSE was calculated only over the four spatially distributed voxels for each metabolite. For example, the tCho RMSEs were calculated over voxels (2, 2), (2, 3), (3, 2) and (3, 3), as illustrated in Fig. 3. Therefore, these RMSEs reflect local changes to the metabolite peak lineshape and amplitude caused by the spatial, spectral aliasing along the k_y–t_1 plane from the NUS and reconstruction.

All of the metabolite RMSEs in the bottom panel of Fig. 5 show similar trends over SNR as the overall RMSEs in the top panel of Fig. 5 at each NUS rate. The MaxEnt and CS reconstructions have lower RMSEs than the zero-augmented datasets, indicating that the metabolite peak lineshapes and amplitudes are being properly reconstructed. The MaxEnt reconstructions have lower RMSEs for many metabolites than the CS reconstructions at higher NUS rates, but, at lower rates, their RMSEs are roughly equivalent.

Figure 6 shows a 1D cross-section of the fully sampled, zero-augmented and reconstructed spectra for high and low SNR simulated spectra at 1.25× and 5× NUS, respectively. The 1D cross-section is indicated by the broken line across F_2 at $F_1 = 3.65$ ppm in Fig. 7, and any NUS artifacts are from aliased peaks above and below the line, not peaks shown in the cross-section. The high SNR, 1.25× NUS zero-augmented spectrum shows only small deviations from the fully sampled spectrum, but they are clearly visible in the inset. Both reconstructions restored the baseline to the level of the fully sampled spectrum and preserved the amplitude and lineshapes of the peaks in the full cross-sections. The artifacts in the low SNR, 5× NUS zero-augmented spectrum show significantly reduced peak amplitudes, broader linewidths and Gibbs ringing along the baseline. Both reconstructions successfully restored the linewidths of the peaks in the full cross-sections and removed the Gibbs ringing shown in the insets; however, MaxEnt was generally better at restoring the peak amplitude as indicated by the red arrows. Many of the real and imaginary peak amplitudes in the CS reconstructions were lower than those of the MaxEnt reconstructions, and the baseline for CS was also slightly lower.

Table 1. Two-dimensional peak locations (ppm) for selected metabolites

	tCho	Glx	Cr	Asp
Diagonals (ppm)	(3.2,3.2), (3.5,3.5), (4.0,4.0), (4.3,4.3)	(2.3,2.3), (3.7,3.7)	(3.0,3.0), (3.9,3.9)	(2.8,2.8), (3.9,3.9)
Cross-peaks (ppm)	(3.5,4.0), (3.5,4.3), (4.0,3.5), (4.3,3.5)	(2.3,3.7), (3.7,2.3)	N/A	(2.8,3.9), (3.9,2.8)

Asp, aspartate; Cr, creatine; Glx, glutamate and glutamine; N/A, not applicable; tCho, total choline (choline + glycerophosphocholine + phosphocholine).
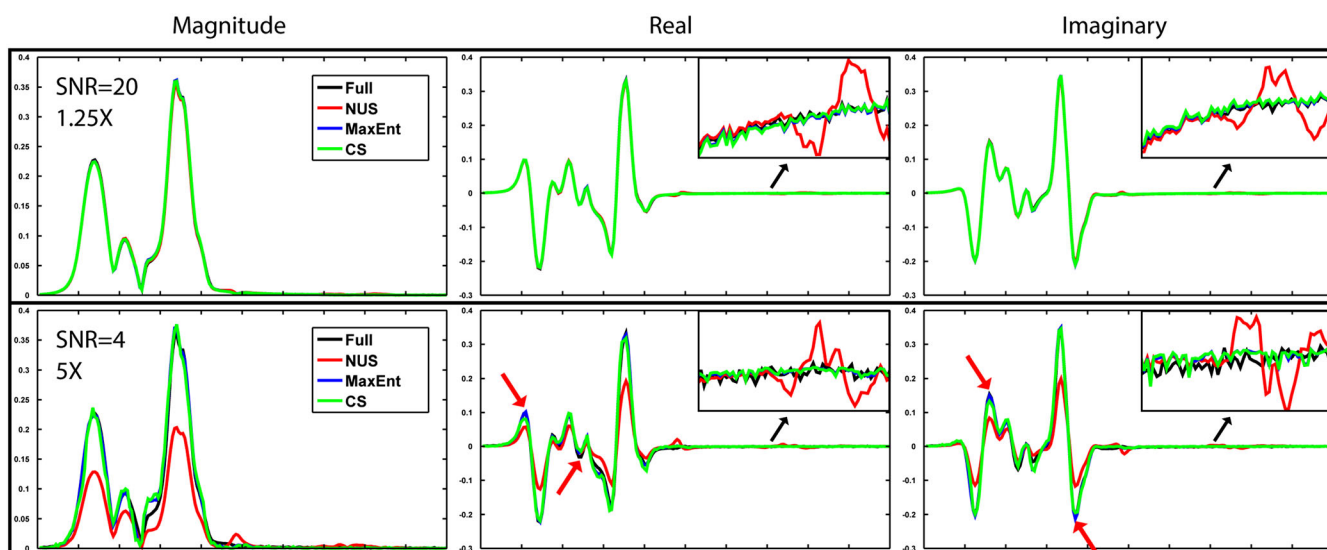

Figure 6. One-dimensional (1D) magnitude, real and imaginary cross-sections of fully sampled, zero-augmented and reconstructed Glx (glutamate and glutamine) spectra. Top: cross-sections from high-signal-to-noise ratio (SNR) spectra 1.25× non-uniform under-sampled (NUS) zero-augmented and reconstructed using maximum entropy (MaxEnt) or compressed sensing (CS). Bottom: cross-sections from low-SNR spectra 5× NUS zero-augmented and reconstructed using MaxEnt or CS. Insets: magnified cross-sections of spectral baselines.
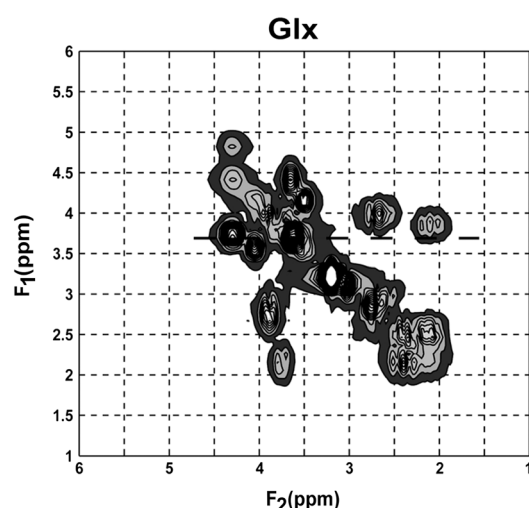

Figure 7. Fully sampled two-dimensional (2D) correlated spectroscopy (COSY) Glx (glutamate and glutamine) spectrum, with the broken line across F_2 at $F_1 = 3.65$ ppm indicating the one-dimensional (1D) cross-section shown in Fig. 6.

NUS of 4D EP-COSI in human breast

The results from a prospective 4× NUS EP-COSI scan of a 31-year-old healthy human breast that was MaxEnt- and CS-reconstructed are shown in Fig. 8A, B, respectively, with the zero-augmented data shown in Fig. 8C. The contour levels employed in the fully sampled results in Fig. 9A were used in Fig. 8. The mask used to under-sample the k_y–t_1 plane is shown in Fig. 4, together with the signal envelopes for each dimension, and was generated using the 2D Poisson-gap method described earlier in this article.

Figure 8A1, B1 shows 2D correlated spectroscopy (COSY) spectra extracted from the MaxEnt and CS reconstructions, respectively. They were taken from the fatty breast regions highlighted in Fig. 8A2, B2. They clearly show the lipid diagonal peaks, olefinic fat (UFD), methyl fat (FMETD) and fat (FAT/FAT2/FAT3), and the cross-peaks, unsaturated fatty acid right (UFR), unsaturated fatty acid left (UFL), and triglyceryl fat (TGFR) (5). The spatial distribution of the UFL/UFR cross-peaks from the reconstructions is shown in Fig. 8A2, B2 with the MaxEnt reconstruction's spatial distribution overlaid on the anatomical MR image.

Figure 8C1 shows the same 2D COSY spectrum as in Fig. 8A1, B1 with 4× NUS applied to the k_y–t_1 plane using the mask in Fig. 4; however, no MaxEnt or CS reconstruction was used. The spatial, spectral incoherent artifacts from NUS manifest as smeared peaks along F_1, which is illustrated by the collapse of the peaks in the 1D projection of the F_1 dimension on the right. The aliasing of the large diagonal fat peaks around ($F_2 = 2$ ppm, $F_1 = 2$ ppm) obscures the much smaller UFL/UFR cross-peaks around ($F_2 = 2.1$ ppm, $F_1 = 5.4$ ppm). Figure 8C2 shows the spatial distribution of the UFL/UFR cross-peaks and how spatial artifacts from the under-sampling of k_y–t_1 manifest as errant peaks in adjacent voxels.
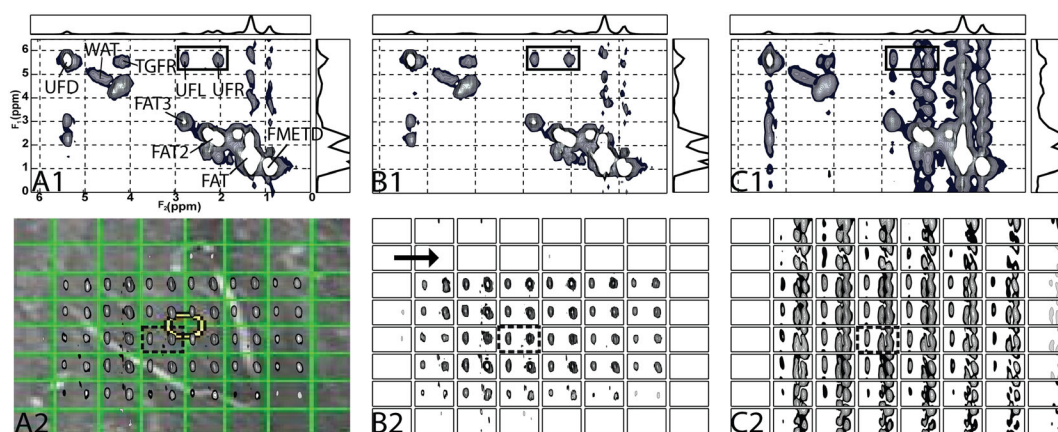
Figure 8. Prospective four-dimensional (4D) echo-planar correlated spectroscopic imaging (EP-COSI) results. Top: selected two-dimensional (2D) correlated spectroscopy (COSY) spectrum from a 4D EP-COSI scan of healthy, fatty breast highlighted in the bottom images for maximum entropy (MaxEnt)-reconstructed (A1), compressed sensing (CS)-reconstructed (B1), and 4× non-uniform under-sampled (NUS) zero-augmented (C1) data. Bottom: spatial distribution of the unsaturated fatty acid left/unsaturated fatty acid right (UFL/UFR) cross-peaks highlighted in the 2D COSY spectrum for MaxEnt-reconstructed (A2), CS-reconstructed (B2), and 4× NUS zero-augmented (C2) data. FAT/FAT2/FAT3, fat; FMETD, methyl fat; TGFR, triglyceryl fat; UFD, olefinic fat.
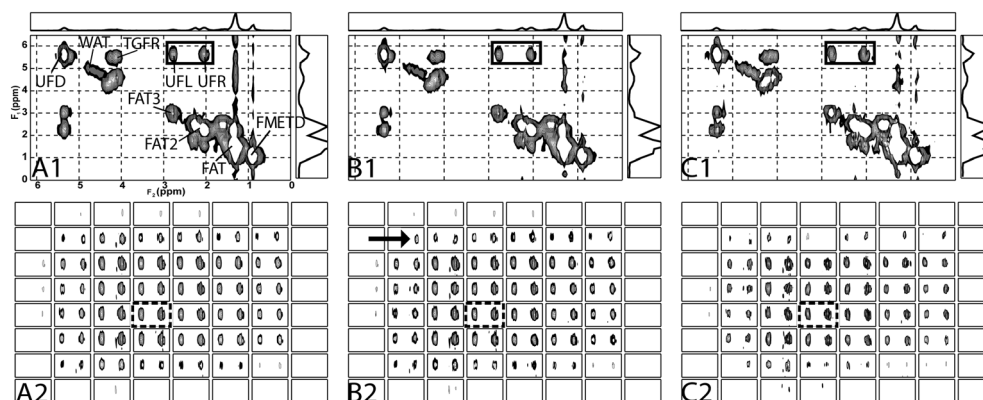

Figure 9. Retrospective four-dimensional (4D) echo-planar correlated spectroscopic imaging (EP-COSI) results. Top: selected two-dimensional (2D) correlated spectroscopy (COSY) spectrum from a 4D EP-COSI scan of healthy, fatty breast highlighted in the bottom images for fully sampled (A1), maximum entropy (MaxEnt)-reconstructed (B1), and compressed sensing (CS)-reconstructed (C1) data. Bottom: spatial distribution of the unsaturated fatty acid left/unsaturated fatty acid right (UFL/UFR) cross-peaks highlighted in the 2D COSY spectrum for fully sampled (A2), MaxEnt-reconstructed (B2), and CS-reconstructed (C2) data. FAT/FAT2/FAT3, fat; FMETD, methyl fat; TGFR, triglyceryl fat; UFD, olefinic fat.

Comparing the MaxEnt- and CS-reconstructed spectra in Fig. 8A1, B1, all of the significant diagonals and cross-peaks are fully resolved in both datasets with qualitatively similar linewidths and amplitudes. The only major differences between them are that the amplitudes of the t_1 ridges centered at ($F_2 = 1.3$ ppm, $F_1 = 1.3$ ppm) and ($F_2 = 1.0$ ppm, $F_1 = 1.0$ ppm) for CS are lower than for MaxEnt.

The results from a fully sampled EP-COSI scan of the same healthy breast as shown in Fig. 8, which was retrospectively 4× under-sampled using the same mask and MaxEnt and CS reconstructions, are illustrated in Fig. 9. Figure 9A shows the fully sampled data and Fig. 9B, C shows the MaxEnt and CS reconstructions, respectively. As the same field of view was used for both scans, the spectra at the top of Fig. 9 show the same 2D COSY spectra as those at the top of Fig. 8, and the bottom shows the spatial distribution of the UFL/UFR cross-peaks. The same contour levels used for the fully sampled data in Fig. 9A were also employed for the MaxEnt- and CS-reconstructed results in Fig. 9B, C.

As can be seen, all of the peaks in the fully sampled spectrum in Fig. 9A1 are completely resolved in both the prospective and retrospective reconstructions shown in Figs 8B1, C1, 9B1, C1; their positions, linewidths, amplitudes and spectral resolutions are all qualitatively comparable. However, the spatial distributions of the fully sampled and retrospective NUS results show better agreement than the prospective NUS results in the upper region of the breast; the excited volume of the prospective NUS results is one row smaller than that of the retrospective NUS results, as indicated by the arrows in Figs 8 and 9. This change was also observed in the non-water-suppressed scans taken prior to the prospective NUS and fully sampled scans, and therefore cannot be an artifact of the reconstruction.

Table 2 shows the F_1 full width at half-maximum (FWHM) and peak amplitudes of the zero-augmented and reconstructed dataset magnitude peaks in Figs 8 and 9. For comparison, they are normalized by the fully sampled peak amplitudes and FWHM from Fig. 9, so that values greater than unity are larger than the fully sampled value. As can be seen, there are quantitative

Table 2. Relative full width at half-maximum (FWHM) along F_1 and amplitude of metabolite peaks for zero-augmented, maximum entropy (MaxEnt)-reconstructed and compressed sensing (CS)-reconstructed data from the voxel shown in Figs 8 and 9. Values are normalized by the fully sampled peak FWHM and amplitudes

	FAT	FAT2	FAT3	FMETD	TGFR	UFD	UFL	UFR
Prospective amplitude								
MaxEnt	1.249	1.342	1.232	1.614	0.951	1.125	1.060	1.078
CS	1.427	1.372	1.263	1.665	0.982	1.142	1.150	1.161
Prospective FWHM								
MaxEnt	0.818	0.909	0.818	1.000	0.818	1.000	0.900	0.727
CS	0.727	0.909	0.818	0.900	0.909	1.000	0.900	0.727
Retrospective amplitude								
Zero-augmented	0.634	0.701	0.662	0.639	0.639	0.627	0.518	0.845
MaxEnt	1.061	1.026	1.090	1.010	1.019	1.029	0.942	0.989
CS	1.237	1.138	1.017	0.961	1.077	0.995	1.071	1.043
Retrospective FWHM								
Zero-augmented	1.273	1.273	1.182	1.30	1.00	1.30	1.40	1.010
MaxEnt	0.818	0.909	0.818	1.00	0.818	1.00	1.00	0.818
CS	0.727	0.818	1.010	1.00	0.727	1.10	0.80	0.727

FAT/FAT2/FAT3, fat; FMETD, methyl fat; TGFR, triglyceryl fat; UFD, olefinic fat; UFL, unsaturated fatty acid left; UFR, unsaturated fatty acid right.

differences between the CS- and MaxEnt-reconstructed peak lineshapes. The zero-augmented dataset has broader, shorter peaks as expected, and both the CS- and MaxEnt-reconstructed peak lineshapes are closer to the fully sampled data; however, the MaxEnt peak lineshapes are almost all closer to the fully sampled data than are the CS peak lineshapes, which are narrower and taller than both the MaxEnt and fully sampled data. The increase in peak amplitudes in the CS reconstruction is greater in the larger peaks (FAT, FAT2 and FAT3) than in the smaller peaks (UFD, UFL, UFR) when compared with MaxEnt.

Additional quantitative differences between the MaxEnt and CS reconstructions are illustrated in Table 3, which shows the range of values for the (UFL + UFR)/(FAT3 + FAT2) integrated peak area ratios and average errors from the fully sampled ratios for the central 6×6 voxels of the three healthy human breasts. As can be seen, NUS caused the ratios to vary considerably from the fully sampled ratios with a high mean ratio error. The reconstructed ratios show much better agreement with the fully

sampled ratios and have a much smaller mean ratio error in all three scans than do the zero-augmented data. However, the mean ratio errors for the MaxEnt reconstruction are almost all smaller than their CS counterparts, indicating that the peak ratio was more accurately reconstructed by MaxEnt. The retrospective reconstruction results are only slightly better than the prospective results, which is not surprising, given the excitation volume differences seen in Figs 8 and 9.

DISCUSSION

The simulated 4D EP-COSI dataset results in Fig. 5 demonstrate how the MaxEnt and CS reconstructions perform at different SNRs and NUS rates. Both reconstructions decrease the RMSE significantly at each SNR and NUS rate, compared with the zero-augmented dataset, but begin to increase at very low SNR, which indicates that they are unable to fully reconstruct

Table 3. Range and mean error of (UFL + UFR)/(FAT3 + FAT2) integrated peak area ratios for fully sampled, zero-augmented, maximum entropy (MaxEnt)-reconstructed, and compressed sensing (CS)-reconstructed data from three healthy breasts

	Ratio range	Mean ratio error	Ratio range	Mean ratio error	Ratio range	Mean ratio error
	Breast 1		**Breast 2**		**Breast 3**	
Full	0.1277–0.0456	N/A	0.1984–0.0656	N/A	0.3542–0.0277	N/A
Zero-augmented	0.2162–0.1496	0.0823 ± 0.0198	0.4699–0.3082	0.2640 ± 0.0734	1.0077–1.1785	0.2047 ± 0.0916
Retrospective MaxEnt	0.1061–0.0281	0.0244 ± 0.0071	0.1576–0.0413	0.0254 ± 0.0142	0.4134–0.0291	0.0215 ± 0.0149
Prospective MaxEnt	0.1049–0.0216	0.0326 ± 0.0083	0.1215–0.0420	0.0415 ± 0.0164	0.3422–0.0414	0.0404 ± 0.0463
Retrospective CS	0.1103–0.0275	0.0246 ± 0.0073	0.1781–0.1004	0.0357 ± 0.0235	0.4114–0.0269	0.0268 ± 0.0175
Prospective CS	0.1084–0.0211	0.0334 ± 0.0082	0.1276–0.0425	0.0397 ± 0.0140	0.3594–0.0374	0.0434 ± 0.0487

FAT2/FAT3, fat; N/A, not applicable; UFL, unsaturated fatty acid left; UFR, unsaturated fatty acid right.

the data when features and sampling artifacts are obscured by high levels of noise. The data fidelity constraint in Equations [1] and [2] determines how closely the reconstructed points must be to the sampled points within the standard deviation of noise, which increases as the noise floor increases. This increase in the noise floor effectively 'loosens' the fidelity constraint, which allows the reconstructed points to deviate from their sampled counterparts and increases the entropy or sparsity of the reconstructed spectrum by narrowing the peak linewidths and de-noising smaller features. This, in turn, increases the non-linearity and RMSE of the reconstruction because of the loose fidelity constraint (41). The data fidelity constraint can be 'tightened' beyond the standard deviation of the noise in an effort to reduce the RMSE and reconstruction non-linearity, but this prevents the Cambridge algorithm from completely removing the spatial, spectral NUS artifacts close to the noise floor, which could potentially obscure small features (21).

The metabolite RMSEs in Fig. 5 show that the reconstructions offer significant improvements in the amplitude and lineshape of individual peaks over the zero-augmented data, even without using methods to reduce the reconstruction non-linearity (32). CS and MaxEnt produce very similar results at low NUS rates, but MaxEnt generally has a lower RMSE at higher NUS rates than this implementation of CS. As demonstrated by Figs 6 and 7, both reconstruction methods successfully restored the peaks and removed the Gibbs ringing artifacts; however, CS had a tendency to over-smooth smaller features close to the noise floor and narrow peak linewidths. It was this over-smoothing that reduced the amplitude of the CS-reconstructed fat tails at ($F_2 = 1.3$ ppm, $F_1 = 1.3$ ppm) and ($F_2 = 1.0$ ppm, $F_1 = 1.0$ ppm) in Fig. 8. The differences in peak linewidths between MaxEnt and CS contributed to the disparity in RMSE values at higher NUS rates, but the main contributing factor was the change in the noise floor in the non-peak regions of the spectra. The noise floor was slightly reduced over the entire 4D dataset in the CS reconstructions, which was the vast majority of points in the volume; therefore, small changes in the noise floor had large effects on RMSE. The over-smoothing in the CS reconstructions may have been caused by choosing $\epsilon = def/1000$ in Equation [4], and will be investigated in the future, although previous work has used similar values with success (13).

The healthy human breast results in Figs 8 and 9 show that CS and MaxEnt reconstructions work well for prospective and retrospective NUS, filtered, *in vivo* EP-COSI scans. There were minor differences between the prospective and retrospective reconstructions; however, these can be attributed to intra-scan variations in the excitation volumes, as these differences were reflected in the MaxEnt and CS reconstructions, as well as in the non-water-suppressed scans. The greater SNR loss caused by T_2^* decay which was not present in the simulated 4D EP-COSI dataset did not reduce the efficacy of the reconstructions. There was still sufficient SNR in the time domain to reconstruct the *in vivo* diagonal and cross-peaks in the spectral domain.

Although the MaxEnt and CS reconstructions of healthy human breast were qualitatively similar, Tables 2 and 3 illustrate quantitative differences between them. Both reconstruction methods improved the ratios of the lipid peaks in Table 3 and the amplitudes and FWHM of major peaks in Table 2, which shows that they were able to reconstruct the large, aliased diagonals, as well as the smaller cross-peaks that were obscured by the diagonals aliasing over the k_y–t_1 plane. However, as shown in Table 2, the CS-reconstructed peaks were narrower with higher amplitudes than their MaxEnt counterparts. This discrepancy increased with

peak amplitude, indicating a higher degree of non-linearity in the CS reconstruction relative to MaxEnt. Using the relative peak amplitudes and FWHM values from Table 2 to calculate the peak area, instead of the integrated peak area that was used for Table 3, the relative (UFL + UFR)/(FAT3 + FAT2) ratios for MaxEnt and CS for the retrospective reconstructions are 0.960 and 0.825, respectively. Because the FAT3 and FAT2 peaks from the CS reconstruction are relatively larger than the MaxEnt peaks from the increased non-linearity, their relative ratio with the UFL and UFR peaks is smaller. This increased non-linearity was a contributing factor in the larger mean ratio errors in Table 3 for the CS reconstructions relative to the MaxEnt reconstructions.

The under-sampled data in Fig. 8C1, C2 show artifacts spread along F_1 and Y, as well as reduced spectral resolution along F_1 and larger FWHMs in Table 2, caused by convolution with the broad NUS PSF. The homogeneous nature of healthy fatty breast spectra, coupled with the inherently low spatial resolution of 4D EP-COSI, made it difficult to determine from the figures whether the spatial resolution along Y decreased as a result of the NUS PSF. However, it is clear that the effects of the NUS PSF along F_1 were removed by MaxEnt and CS by the narrower FWHM values in Table 2 and the lack of NUS artifacts in Figs 8A1, B1, 9A1, B1. The errant spectral peaks in the spatial distribution were removed in Figs 8A2, B2, 9A2, B2, suggesting that the spatial PSF along Y was also improved. Any spectral bleed from the spatial PSF of the EP-COSI pulse sequence along X was orthogonal to the effect of the NUS PSF along Y, and was not affected by the MaxEnt and CS reconstructions.

The results in Figs 5–9 indicate that MaxEnt and CS produced qualitatively similar reconstructions; however, the MaxEnt results were quantitatively better by a small margin as discussed above. This is not surprising, given that the objective functions of CS and MaxEnt are similar, but there are minor differences between them as shown in Fig. 1. CS uses the l_1-*norm* of the reconstructed spectrum in some transform domain, and MaxEnt uses entropy, which is a log-sum function that can be rewritten as a reweighted l_1-*norm*, $\sum w_i \cdot |m_i|$, where w_i is $\log[f(m_i)]$, the log of a function of the reconstructed spectrum. Previous work has shown that reweighted l_1-*norm* objective functions can outperform l_1-*norm*-based CS reconstruction (42), and direct comparisons between MaxEnt and l_1-*norm*-based CS reconstruction have shown them to be qualitatively equivalent (43). This is the first known work to show quantitative comparisons between these techniques, however, and further research into their relative performance is ongoing.

The Cambridge algorithm used to solve the MaxEnt and CS reconstruction problems was demonstrated to be robust against different levels of SNR and NUS rates for the simulated and *in vivo* datasets. There are other l_1-*norm* solvers available for the CS reconstruction problem; however, many require parameter tuning for different datasets in order to find the optimal reconstruction parameters (44,45). The Cambridge algorithm does not have any tuning parameters that must be adjusted to find the optimal reconstruction for a dataset, which offers a substantial workflow improvement over other solvers. Although the Cambridge algorithm can be modified to solve the CS l_1-*norm* reconstruction problem, it takes, on average, 5–10 times longer to converge as the MaxEnt problem, which took 7–10 min, on average, using a 64-bit dual-core, 3.4-GHz Core i7 processor with 16GB RAM. Therefore, we do not recommend its use as an l_1-*norm* solver; it was only used for the current work in order to compare results for MaxEnt and CS reconstruction that were not biased by different solver implementations. However,

because it is relatively fast, robust to SNR changes, does not require parameter tuning, and provides MaxEnt results that were equal to or better than those of CS, the Cambridge algorithm is well suited as a MaxEnt solver.

The Poisson-gap sampling masks used in these experiments were generated by a random Poisson distribution, which injects a degree of uncertainty into the reconstruction. It has proven to be a reliable technique that generates masks with desirable PSFs, as shown in Fig. 2, and the RMSEs of the reconstructed datasets using different Poisson-gap sample masks are stable (28). Previous attempts by our group to use deterministic masks that were not randomly generated were difficult to optimize and suffered from coherent aliasing, which cannot be removed by MaxEnt or CS reconstruction (32,46). Recent work in NUS multi-dimensional NMR datasets using deterministic sample masks has shown promise and could be adapted to 4D MRSI (47).

Because of the random nature of the Poisson-gap sampling masks, they were chosen by an empirical heuristic that minimized the width of the central peak, the total power of the incoherent artifacts, and the ratio of the largest artifact peak to the central peak in the mask PSF. They followed a skewed-sine bell modulation function to maximize the reconstruction SNR, but were not optimized for specific metabolites or post-processing spectral filters. In our experiments, we observed that mismatches between a sample modulation function and the filtered signal envelope of a metabolite results in failure to sufficiently sample the high-SNR points along t_1 and prevents the full metabolite peak area from being reconstructed (31,32,48). Therefore, it should be emphasized that the sample mask is crucial to the SNR of each reconstructed metabolite for 4D EP-COSI data, and there is a dependence on the shape of standard spectral filters applied prior to reconstruction (33).

Further research into reducing the non-linearity of the reconstructed peaks to make accurate quantification possible, and comparisons with additional CS methods, is ongoing. In addition, future papers will address the use of Poisson-gap versus deterministic sample masks, and the optimization of the modulation functions for specific metabolites and different spectral filters.

CONCLUSIONS

This work has demonstrated that MaxEnt is a viable alternative to l_1-norm-based CS reconstruction for accelerating the acquisition of 4D EP-COSI data *in vivo*. MaxEnt provided reconstructions equal to or better than those of CS, and the robust nature of the Cambridge algorithm without the need for parameter tuning makes it a good candidate for clinical use. The CS and MaxEnt reconstructions throughout this work were qualitatively similar; however, the quantitative results indicated increased non-linearity in the CS reconstruction when compared to MaxEnt. Simulated 4D EP-COSI data provided a quantitative characterization of both reconstruction methods at different NUS rates and SNRs, and the 4× NUS *in vivo* EP-COSI breast data showed that a clinically viable 5-min breast scan is possible.

Acknowledgements

REFERENCES

1. Thomas MA, Lipnick S, Velan SS, Liu X, Banakar S, Binesh N, Ramadan S, Ambrosio A, Raylman RR, Sayre J, DeBruhl N, Bassett L. Investigation of breast cancer using two-dimensional MRS. NMR Biomed. 2008; 22(1): 77–91.
2. Begley JK, Redpath TW, Bolan PJ, Gilbert FJ. In vivo proton magnetic resonance spectroscopy of breast cancer: a review of the literature. Breast Cancer Res. 2012; 14(2): 207.
3. Glunde E, Bhujwalla ZM, Ronen SM. Choline metabolism in malignant transformation. Nat Rev Cancer, 2011; 11(2): 835–848.
4. Aue W, Bartholdi E, Ernst R. Two-dimensional spectroscopy. Application to nuclear magnetic resonance. J. Chem. Phys. 1976; 64: 2229–2246.
5. Lipnick S, Liu X, Sayre J, Bassett LW, DeBruhl N, Thomas MA. Combined DCE-MRI and single-voxel 2D MRS for differentiation between benign and malignant breast lesions. NMR Biomed. 2010; 23(8): 922–930.
6. Mansfield P. Spatial mapping of the chemical shift in NMR. J Phys D Appl Phys 1983; 16: 235–238.
7. Mulkern R, Panych L. Echo planar spectroscopic imaging. Concepts Magn. Reson. 2001; 13: 213–237.
8. Posse S, DeCarli C, Le-Bihan D. 3D echo planar spectroscopic imaging at short echo times in human brain. Radiology 1994; 192: 733–738.
9. Lipnick S, Verma G, Saadallah R, Jon F, Thomas MA. Echo planar correlated spectroscopic imaging: implementation and pilot evaluation in human calf in vivo. Magn Reson Med 2010; 64(4): 947–956.
10. Furuyama JK, Wilson NW, Burns BL, Rajakumar N, Margolis D, Thomas MA. Application of compressed sensing to multidimensional spectroscopic imaging in human prostate. Magn Reson Med 2012; 67: 1499–1505.
11. Donoho D. Compressed sensing. IEEE Trans. Info. Theor. 2006; 52(4): 1289–1306.
12. Candes EJ, Romberg J, Tao T. Robust uncertainty principles: exact signal reconstruction from highly incomplete frequency information. IEEE Trans. Info. Theor. 2006; 52(2): 489–509.
13. Lustig M, Donoho D, Pauly JM. Sparse MRI: the application of compressed sensing for rapid MR imaging. Magn Reson Med 2007; 53(6): 1182–1195.
14. Block KT, Uecker M, Frahm J. Undersampled radial MRI with multiple coils. Iterative image reconstruction using a total variation constraint. Magn Reson Med 2007; 57(6): 1086–1098.
15. Hu S, Lustig M, Chen A, Crane J, Kerr A, Kelley DAC, Hurd R, Kurhanewicz J, Nelson SJ, Pauly JM, Vigneron DB. Compressed sensing for resolution enhancement of hyperpolarized C13 flyback 3D-MRSI. J Magn Reson 2008; 192: 258–264.
16. Gamper U, Boesiger P, Kozerke S. Compressed sensing in dynamic MRI. Magn Reson Med 2008; 59: 365–373.
17. Jung H, Kyunghyun S, Nayak KS, Kim E, Ye JC. k-t FOCUSS: a general compressed sensing framework for high resolution dynamic MRI. Magn Reson Med 2009; 61(1): 103–116.
18. Frieden RB. Restoring with maximum likelihood and maximum entropy. J Opt Soc Am 1972; 62(4): 511–518.
19. Skilling J, Bryan RK. Maximum entropy image reconstruction: general algorithm. Monthly Notices R. Astronom. Soc. 1984; 211(1): 111–124.
20. Daniell GJ, Hore PJ. Maximum entropy and NMR–a new approach. J Magn Reson. 1989; 4(3): 515–536.
21. Hoch J, Stern AS. *NMR Data Processing*. Wiley: New York, NY; 1996.
22. Jaynes ET. Information theory and statistical mechanics. Phys Rev 1957; 106(4): 620–630.
23. Holland D, Bostock M, Gladden L, Nietlispach D. Fast multidimensional NMR spectroscopy using compressed sensing. Angew Chem Int Ed 2011; 50(29): 6548–6551.
24. Boyd S, Vandenberghe L. *Convex Optimization*. Cambridge University Press: Cambridge, 2004.
25. Shannon CE. A mathematical theory of communication. Bell Sys. Tech. J. 1948; 27: 379–423, 623–656.
26. Frieden R. Unified theory for estimating frequency-of-occurrence laws and optical objects. J Opt Soc Am 1983; 73(7): 927–938.
27. Constable RT, Henkelmen RM. Why MEM does not work in MR image reconstuction. Magn Reson Med 1990; 14: 12–25.
28. Hyberts SG, Takeuchi K, Wagner G. Poisson-gap sampling and forward maximum entropy reconstruction for enhancing the resolution and senstivity of protein NMR. J Am Chem Soc 2010; 132: 2145–2147.
29. Maciejewski MW, Mobli M, Schuyler A, Stern A, Hoch J. Data sampling in multidimensional NMR: fundamentals and strategies. Top Curr Chem 2011; 316: 49–77.
30. Silverman H, Shapiro R. Alias free sampling of random noise. SIAM J. 1960; 8(2): 225–248.

31. Mobli M, Hoch JC. Maximum entropy spectral reconstruction of nonuniformly sampled data. Concepts Magn. Reson. 2008; 32A(6): 436–448.

32. Schmieder P, Stern A, Wagner G, Hoch J. Applications of nonlinear sampling schemes to COSY-type spectra. J Biomol NMR 1993; 3(5): 569–576.

33. Ziegler A, Izquierdo M, Decorps M. Optimization of homonuclear two-dimensional correlation methods for in vivo and ex vivo NMR. J. Magn. Reson. Ser. B 1995; 107: 10–18.

34. Marseille GJ, De Beer R, Fuderer M, Mehlkopf AF, van Ormondt D. Nonuniform phase-encode distributions for MRI scan time reduction. J. Magn. Reson. Ser. B 1996; 111: 70–75.

35. Devroye L. *Non-Uniform Random Variate Generation*. Springer-Verlag: New York, NY; 1986.

36. Dippe M, Wold E. Antialiasing through stochastic sampling. ACM SIGGRAPH Comp. Graphics 1985; 19(3): 69–78.

37. Cook R. Stochastic sampling in computer graphics. ACM Trans. Comp. Graphics 1986; 5(1): 51–72.

38. Smith SA, Levante TO, Meier BH, Ernst RR. Computer simulations in magnetic resonance. an object-oriented programming approach. J Magn Reson 1994; 106(1): 75–105.

39. Thomas MA, Yue K, Binesh N, Davanzo P, Kumar A, Siegel B, Frye M, Curran J, Lufkin R, Martin P, Guze B. Localized two-dimensional shift correlated MR spectroscopy of human brain. Magn Reson Med 2001; 46(1): 58–67.

40. Pierpaoli C, Basser PJ. Toward a quantitative assesment of diffusion anisotropy. Magn Reson Med 1996; 36: 893–906.

41. Hoch J, Stern A, Donoho D, Johnstone IM. Maximum entropy reconstruction of complex (phase-sensitive) spectra. J Magn Reson 1990; 86: 236–246.

42. Candes E, Wakin M, Boyd S. Enhancing sparsity by reweighted l1 minimization. J. Fourier Anal. Appl. 2008; 14: 877–905.

43. Stern A, Donoho D, Hoch J. NMR data processing using iterative thresholding and minimum l1-norm reconstruction. J Magn Reson 2007; 188: 295–300.

44. Chen SS, Donoho DL, Saunders MA. Atomic decomposition by basis pursuit. Siam J. Sci. Comput. 1998; 20(1): 33–61.

45. Kim SJ, Koh K, Lustig M, Boyd S, Gorinevsky D. An interior-point method for large-scale l1-regularized least squares. IEEE J. Sel. Topics Signal Process. 2007; 1(4): 606–617.

46. Barna J, Laue E, Mayger M, Skilling J, Worrall S. Exponential sampling, an aternative method for sampling in two-dimensional NMR experiments. J Magn Reson 1987; 73: 69–77.

47. Eddy M, Ruben D, Griffin R, Herzfeld J. Deterministic schedules for robust and reproducible non-uniform sampling in multidimensional NMR. J Magn Reson 2012; 214: 296–301.

48. Schmeider P, Stern A, Wagner G, Hoch J. Quantification of maximum-entropy spectrum reconstructions. J Magn Reson 1997; 125: 332–339.

Copyright © 2013 John Wiley & Sons, Ltd.
wileyonlinelibrary.com/journal/nbm

SPLIT-BREGMAN-BASED GROUP-SPARSE RECONSTRUCTION OF MULTIDIMENSIONAL SPECTROSCOPIC IMAGING DATA

Brian Burns[*], *Neil Wilson*[†], *M. Albert Thomas*[*†]

[*] Department of Biomedical Engineering, UCLA, Los Angeles, CA 90025 USA
[†]Bio-Medical Physics IDP, UCLA, Los Angeles, CA 90025 USA

ABSTRACT

4D Magnetic Resonance Spectroscopic Imaging data provides valuable biochemical information *in vivo*, however, its acquisition time is too long for a clinical protocol. In this paper, 4D simulated MRSI data at PSNRs=20, 10, 5 are under-sampled 2X, 4X, 6X, or 8X and reconstructed with Compressed Sensing and Group Sparsity. A Group Sparse problem solution within the Split-Bregman framework is derived, which allows for arbitrary, over-lapping grouping structures. Preliminary results show that Group Sparse metabolite peak amplitudes and line width reconstructions are more accurate than Compressed Sensing reconstructions.

Index Terms— Group Sparsity, Compressed Sensing, Split Bregman, Convex Optimization, Spectroscopic Imaging

1. INTRODUCTION

Magnetic Resonance Imaging (MRI) exploits the resonant frequency of ^{1}H protons within water *in vivo* to generate anatomical images of the human body. Magnetic Resonance Spectroscopic Imaging (MRSI) is a similar imaging technique to MRI, however in lieu of the resonant frequency of ^{1}H protons in water, the resonant frequencies of ^{1}H protons in metabolites are used to generate a metabolic image instead. Each metabolites has a unique resonance spectrum *in vivo* caused by their molecular bonding structure, which can be used to identify and quantify their concentrations within each voxel. Using this concentration information, the biochemical compositions of healthy and diseased tissues can be determined without the need for invasive biopsies and the altered metabolism of cancers can be detected [1].

The Echo-Planar Correlated Spectroscopic Imaging (EP-COSI) MRSI pulse sequence allows for the simultaneous acquisition of two spatial and two spectral dimensions, (k_y, k_x, t_2, t_1), in one scan *in vivo* [1]. This 4D sequence provides a 2D spectrum for each voxel in a slice. The overlap of resonance peaks within a single spectral dimension is a major impediment to identifying individual metabolites and

the increased spectral dispersion offered by a second spectral dimension can disentangle complex over-lapping spectral peaks. However, 4D MRSI acquisitions are slow compared to most MRI sequences and can take up to 40 minutes, which is too long to be used on a routine clinical basis.

4D EP-COSI data acquisition is a rasterized scan that acquires a 2D spatiotemporal plane, $k_x - t_2$, from the 4D volume during each repetition time (TR). The second spatial (k_y) and spectral (t_1) dimensions are incrementally acquired between rasters until the entire 4D volume is sampled. k_y is incrementally acquired using standard phase encoding techniques from MRI and t_1 is incrementally acquired as a series of 1D spectra with modified timings [1]. To accelerate the collection of 4D EP-COSI data *in vivo* the incrementally acquired dimensions, k_y and t_1, can be non-uniformly undersampled (NUS). However, NUS produces artifacts that must be removed by reconstructing the missing samples in the $k_y - t_1$ plane through non-linear, iterative reconstruction [2].

Previous work has demonstrated the feasibility of under-sampling the mixed-domain $k_y - t_1$ plane of a 4D MRSI data set and reconstructing the missing samples with Compressed Sensing (CS), Total Variation (TV) denoising, and Maximum Entropy (MaxEnt) [3, 4]. NUS rates as low as 5X were demonstrated *in vivo* and showed that it is possible to accelerate the acquisition of 4D MRSI data down to a clinically acceptable 5-10 minutes. The current work uses the Group Sparse (GS) reconstruction method to reconstruct simulated 4D EP-COSI data sets at different NUS rates and PSNRs using the Split-Bregman iterative reconstruction algorithm [5, 6]. The Split-Bregman algorithm has been modified to allow for arbitrary transform coefficient grouping patterns of overlapping or non-overlapping groups and can successfully reconstruct NUS MRSI data sets down to 8X. The Split-Bregman algorithm has been previously used for TV-based reconstruction of NUS MRSI data [3] and for multi-channel reconstruction of NUS MRI data by extending the algorithm to accomodate row-wise grouping of jointly sparse samples [7].

2. THEORY

2.1. Split Bregman Algorithm

The Split-Bregman algorithm is from the class of Alternating Direction Method of Multipliers (ADMM) that split a con-

strained problem into a sequence of simpler unconstrained sub-problems [6]. It differs from continuation-based methods by keeping the values of any Lagrange multipliers fixed between iterations and modifies the data instead. This has the benfits of increased numerical stablity and a lower dependence on the initial Lagrange multiplier values. If we wish to use the Split Bregman algorithm to solve the problem:

$$
\begin{aligned}
\min_{u,z} \quad & E(u,z) \\
\text{such that} \quad & H(u,z)
\end{aligned}
\tag{1}
$$

where $E(u,z)$ is a convex, non-differentiable function and $H(u,z)$ can be assumed to be of the form $Au = z$. We first convert it to an unconstrained problem:

$$
\min_{u,z} E(u,z) + \lambda H(u,z)
\tag{2}
$$

where conventional continuation-based methods would increase $\lambda \to \infty$ to find a solution; however, we apply the Bregman distance relaxation to equation 2 and split it into sub-problems instead. The Bregman distance for the function $E(u)$ at the point u^k is:

$$
D_E^p(u,u^k) = E(u) - E(u^k) - \langle p_u^k, u - u^k \rangle
\tag{3}
$$

where p_u^k is the subgradient of $E(u)$ at u^k. The Bregman distance and iteration scheme are then applied to equation 2:

$$
\begin{aligned}
(u^{k+1}, z^{z+1}) &= \min_{u,z} D_E^p(u,u^u,z,z^k) + \lambda H(u,z) \\
p_u^{k+1} &= p_u^k - \lambda \nabla_u H(u^{k+1}, z^{k+1}) \\
p_z^{k+1} &= p_z^k - \lambda \nabla_z H(u^{k+1}, z^{k+1})
\end{aligned}
\tag{4}
$$

which is iterated over k until convergence. λ is never increased and under fairly weak assumptions on $E(u,z)$ and $H(u,z)$, $\nabla_u H$ and $\nabla_z H \to 0$ as $k \to \infty$ so that $p^{k+1} \to p^k$ and the Bregman parameters converge [6]. However, because $H(u,z)$ is of the form $Au = z$, equation 4 can be simplified:

$$
\begin{aligned}
(u^{k+1}, z^{z+1}) &= \min_{u,z} E(u,z) + \lambda \| z - Au - b^k \|_2^2 \\
b^{k+1} &= b^k + Au^{k+1} - z^{k+1}
\end{aligned}
\tag{5}
$$

where b^{k+1} is a Bregman parameter that ensures $Au \to z$ as the iterations converge without increasing λ and sacrificing stability. Because $E(u,z)$ is convex and non-differentiable, equation 5 is split into u and z subproblems, which are solved independently at each iteration, decoupling u from z:

$$
\begin{aligned}
u^{k+1} &= \min_u E(u,z^k) + \lambda \| z^k - Au - b^k \|_2^2 \\
z^{z+1} &= \min_z E(u^k + 1, z) + \lambda \| z - Au^{k+1} - b^k \|_2^2 \\
b^{k+1} &= b^k + Au^{k+1} - z^{k+1}
\end{aligned}
\tag{6}
$$

2.2. Group Sparse Reconstruction

GS reconstruction is an extension of CS that exploits the correlations among adjacent transform coefficients caused by their structured sparsity [5]. Structured sparsity is the tendency of large transform coefficients to be adjacent to eachother and form clusters. In GS reconstruction, adjacent transform coefficients are reconstructed together in groups rather than individually, as is done in CS. By reconstructing groups of coefficients, the GS signal model correlates individual transform coefficients with their neighbors allowing them to influence eachother.

GS reconstruction can be formed as a constrained convex optimization problem that uses the $l_{1,2}$-norm as the objective function instead of the l_1-norm used in CS. The $l_{1,2}$-norm is:

$$
\| z \|_{1,2} = \| z_{g1} \|_2 + \| z_{g2} \|_2 + \ldots + \| z_{gL} \|_2
\tag{7}
$$

where $z_{gi} \in \mathbb{C}^P = \{u_j, u_l \ldots u_n\}$ and $j,k,n \in \{S = 1 \ldots N, P \leq N\}$ is a group of transform coefficients from u. The MRSI GS reconstruction problem is then defined as:

$$
\begin{aligned}
\min_{u,z} \quad & \| z \|_{1,2} \\
\text{such that} \quad & \| R\mathcal{F}u - f \| \leq \sigma \\
& z = Gu
\end{aligned}
\tag{8}
$$

where $u = (Y, X, F_2, F_1)$ is the reconstructed spatial, spectral-domain data, $\mathcal{F}$ is the 4D Fourier operator, R is the under-sampling mask that determines which samples were acquired in the $k_y - t_1$ plane, $f = (k_y, k_x, t_2, t_1)$ is the sampled k-space, time-domain data, G is the group matrix of 1s and 0s that determines which coefficients from u belong to each group in z [8], and σ is the standard deviation of the noise in f. The SB problem reduces to the CS problem when each group contains one coefficient and $G = I$. Because each transform coefficient may be within more than one group and separate reconstructions must be created for each version of that coefficient, the set of transform coefficient groups, z, may contain more points than u.

2.3. Split-Bregman Based Group Sparse Reconstruction

The MRSI GS reconstruction problem can be solved by the Split-Bregman algorithm by defining equation 8 as an unconstrained problem:

$$
\min_{u,z} E(u,z) + \lambda H(u,z)
\tag{9}
$$

where

$$
\begin{aligned}
E(u,z) &= \| z \|_{1,2} + \mu \| R\mathcal{F}u - f \|_2^2 \\
H(u,z) &= \| z - Gu \|_2^2
\end{aligned}
\tag{10}
$$

By following the process defined in equations 4-6, we can derive u and z sub-problems and a Bregman parameter update that solves the unconstrained problem in 9:

$$
\begin{aligned}
u^{k+1} &= \min_u \mu \| R\mathcal{F}u - f^i \|_2^2 + \lambda \| z^k - Gu - b_z^k \|_2^2 \\
z^{z+1} &= \min_z \| z \|_{1,2} + \lambda \| z - Gu^{k+1} - b_z^k \|_2^2 \\
b_z^{k+1} &= b_z^k + Gu^{k+1} - z^{k+1}
\end{aligned}
\tag{11}
$$

where μ and λ are Lagrange multipliers. The z^{k+1} sub-problem is non-differentiable, however, its equivalent problem can be solved:

$$
\begin{aligned}
z^{k+1} &= \min_z \sum_{i=1}^L \left[\| z_{gi} \|_2 + \lambda \| z_{gi} - (Gu^{k+1})_{gi} - (b_z^k)_{gi} \|_2^2 \right] \\
&= gshrink(Gu^{k+1} + b_z^k, \tfrac{1}{\lambda}, G)
\end{aligned}
\tag{12}
$$

where $gshrink$ is group-wise shrinkage over each group [8]. Because the u^{k+1} sub-problem is differentiable, optimality conditions can be derived for u and simplified to:

$$(\mu \mathcal{F}' R' R \mathcal{F} + \lambda G' G) u^{k+1} = \mu \mathcal{F}' R' f^i + \lambda G' \left(z^k - b_z^k \right) \tag{13}$$

where $G'G$ is a diagonal matrix with each $(G'G)_{ii}$ the number of groups that contain transform coefficient u_i^{k+1} [8]. If each transform coefficient is in the same number of groups, so $G'G$ is a multiple of I, the left-hand side of equation 13 is circulant and can be inverted by the Fourier transform:

$$u^{k+1} = \mathcal{F}' K^{-1} \mathcal{F} \left(\mu \mathcal{F}' R' f^i + \lambda G' \left(z^k - b_z^k \right) \right) \tag{14}$$

where $K = (\mu R' R + \lambda G' G)$ is diagonal. If each transform coefficient is not in the same number of groups and $G'G$ is not a multiple of I, u^{k+1} in equation 13 can be solved for by the Gauss-Seidel method.

Iterating the sub-problems and Bregman update over k in equation 11 solves the unconstrained problem; however, to solve the constrained problem in equation 8, an outer iteration is completed over i that updates f based on changes to u^{k+1}:

$$f^{i+1} = f^i + \left(f - R\mathcal{F} u^{k+1} \right) \tag{15}$$

The number of iterations over k is application dependent, but for the MRSI GS problem, we use 15 iterations over k for each iteration over i and iterate over i until the normalized residual error between u^{k+1} and f^i is less than $10e^{-5}$.

3. METHODS

CS and GS reconstructions were quantitatively compared using a simulated 4D EP-COSI data set that contained *in vivo* concentrations of the metabolites: Aspartate, Choline, Creatine, GABA, Glutamate, Glutamine, Glucose, Lactate, Myo-Inositol, and N-acetyl-aspartate. The 2D spectrum of each metabolite was simulated using the GAMMA NMR libraries with the following parameters: 100 t_1, 1024 t_2, TR/TE= 1.5s/30ms, and spectral bandwidths of 1250Hz and 2000Hz along F_1 and F_2, respectively. Each 2D spectrum was line-broadened by 10 Hz to simulate *in vivo* conditions then apodized by a sine-squared filter along t_1 and a skewed sine-squared filter with skew parameter 0.5 along t_2. They were then copied into the central 6x6 region of a 16x16 spatial grid to simulate a spatial distribution.

Noise was added to the simulated noise free 4D EP-COSI data set to model PSNRs of 20, 10, and 5. The SNR was varied by adding univariate Gaussian noise to the noise-free real and imaginary channels of the 4D EP-COSI data. It was under-sampled 8X, 6X, 4X, and 2X and then separately reconstructed by CS, GS with non-overlapping groups (GS_1), and GS with over-lapping groups (GS_2). The group sizes used in (GS_1) and (GS_2) were $(t_1, t_2) = (4, 16)$, which were empirically determined. The CS problem was solved by making the group size one coefficient, $(t_1, t_2) = (1, 1)$. Because the noise was random, each SNR was simulated and reconstructed 50 times per NUS rate.

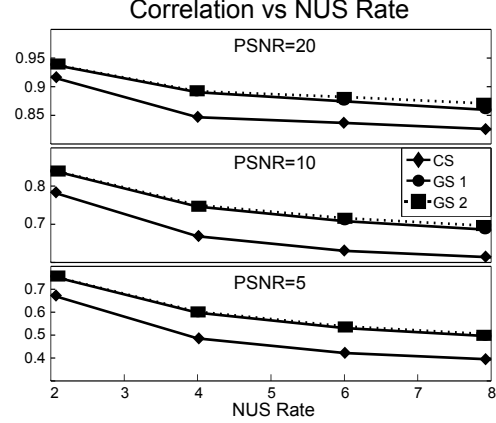## 4. RESULTS AND DISCUSSION

Fig. 1. The mean linear correlation coefficient between the fully sampled and reconstructed 4D EP-COSI data sets after 8X, 6X, 4X, 2X NUS at PSNRs of 20, 10, 5

The mean linear correlation coefficients between the reconstructions and the fully sampled simulated 4D EP-COSI data set are shown in figure 1. Values were calculated from the 50 reconstructions performed at each PSNR and NUS rate. Error bars are not shown because the standard deviations were three to four orders of magnitude smaller than the mean correlation coefficients. The linear correlation coefficient is a measure of the strength of the linear relationship between two vectors; two vectors are strongly correlated for values close to 1 and -1. As can be seen in figure 1, both the GS reconstructions have higher mean correlation coefficients than the CS reconstructions for all PSNR values and NUS rates tested. Additionally, the GS_2 reconstructions have higher mean correlation values than the GS_1 reconstructions at higher NUS rates and this difference increases with PSNR. This suggests the metabolite peak line-shapes and amplitudes are more accurately reconstructed by the GS reconstructions than CS.

Figure 2 shows a representative 2D spectrum from the simulated 4D EP-COSI data set at PSNR=5. The left shows the fully sampled spectrum followed by the 8X NUS spectrum in the next column, then the CS and GS reconstructions. The bottom of figure 2 shows a cross section of each 2D spectrum as indicated by the vertical dotted line in the fully sampled spectrum. In each cross section, the fully sampled peaks are plotted in dark gray and the NUS and reconstructed peaks are in black. Both GS reconstructions restored each of the metabolite peaks to their fully sampled amplitudes and widths, as well as reduced the noise floor below that of the fully sampled spectrum. The CS reconstructed Glx peak is smaller than the fully sampled peak and the GABA peak amplitude is larger, while the NAA peak is restored to its original amplitude and line-width. This indicates a higher degree of non-linearity in the CS reconstruction than the GS reconstructions, which may have adverse effects on metabolite concentrations estimates that rely on relative peak areas.
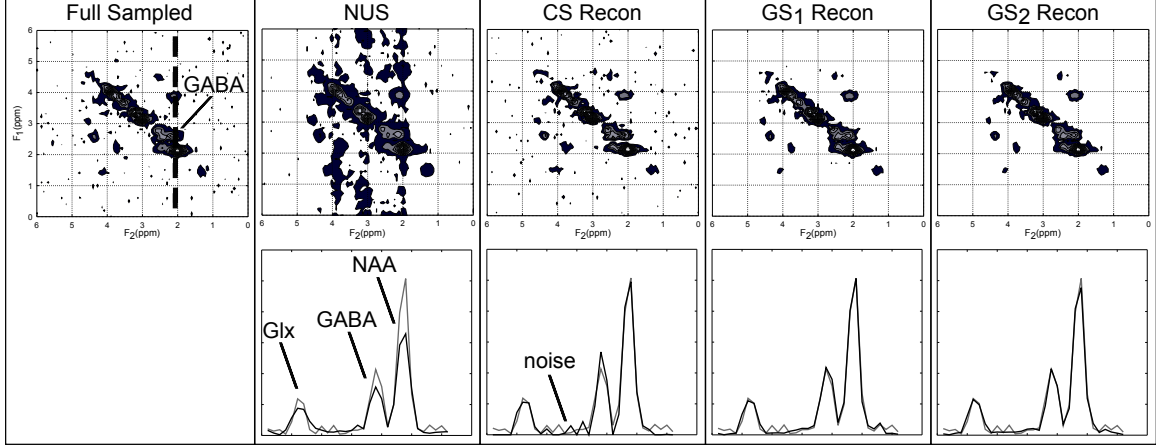
Fig. 2. (Top) Representative 2D spectrum from simulated 8X NUS 4D EP-COSI data set with a PSNR=5 (Bottom) 1D cross-section indicated by dotted line on fully-sampled spectrum showing the Glx, GABA, and NAA peaks for the NUS or reconstructed spectrum in black and the fully sampled spectrum in dark gray

The effects of the reconstruction on the GABA cross peak are illustrated in table 1. The mean amplitudes and Full-Width Half Maximums (FWHM) along F_1 for the metabolite peak with respect to the fully sampled values are given for the 4X and 8X NUS data sets, and the CS and GS reconstructions for PSNRs=20, 10, 5. Values were calculated from the 50 reconstructions as in figure 1. As was seen in figure 2, the CS reconstructed GABA peak is larger and narrower than the fully sampled peak at each PSNR and NUS rate. The GS reconstructions were better able to reconstruct the GABA metabolite peak to the appropriate amplitude and FWHM. The GS_2 reconstructions show a trend of better relative performace to the other reconstruction methods at high NUS rates and PSNRs, which was also seen in figure 1.

	PSNR=20		PSNR=10		PSNR=5		
	4X	8X	4X	8X	4X	8X	
NUS	0.733	0.612	0.730	0.608	0.726	0.601	Amplitude
CS	1.092	1.043	1.100	1.035	1.128	1.035	
GS₁	0.986	0.944	0.977	0.933	0.958	0.894	
GS₂	1.025	1.01	1.011	0.987	0.982	0.936	
NUS	1.018	1.128	1.032	1.121	1.047	1.112	FWHM
CS	0.897	0.913	0.850	0.891	0.780	0.842	
GS₁	0.958	0.966	0.980	0.973	1.008	0.985	
GS₂	0.973	0.977	0.975	0.974	0.975	0.970	

Table 1. GABA cross peak amplitude and F_1 FWHM relative to fully sampled values.

The Split-Bregman GS problem converges in fewer iterations than the CS problem, but takes more time to compute per iteration because of group-wise shrink. The current Matlab implementation of GS takes 2-3 times longer to converge than CS and is a current topic of research.

5. CONCLUSION

This work shows that GS reconstruction of 4D MRSI data sets is a viable alternative to CS-based methods. The Split-Bregman-based GS algorithm was developed and evaluated on simulated data sets at varying PSNRs and NUS rates. GS reconstruction results demonstrated better metabolite peak reproduction and lower non-linearity than CS. Further work is required to determine the optimal grouping strategy under different experimental conditions.

6. REFERENCES

[1] S Lipnick et al, "Ep-cosi: implementation and pilot evaluation in human calf in vivo," *Magn. Reson. Med.*, vol. 64, pp. 947–956, 2010.

[2] M Lustig et al, "Compressing sensing in mri," *IEEE Signal Process. Mag.*, vol. 25, pp. 72–82, 2008.

[3] JK Furuyama et al, "Application of cs to multidimensional spectroscopic imaging in human prostate," *Magn. Reson. Med.*, vol. 67, pp. 1499–1505, 2012.

[4] BL Burns et al, "Non-uniformly under-sampled multidimensional spectroscopic imaging in vivo: Maximum entropy versus compressed sensing reconstruction," *NMR in BioMed*, vol. in press, 2013.

[5] M Yuan and Y Lin, "Model selection and estimation in regression with grouped variables," *Statist. Soc. B.*, vol. 68, pp. 49–67, 2006.

[6] T Goldstein and S Osher, "The split bregman method for l1-regularized problems," *SIAM J. Imaging Sci.*, vol. 2, pp. 323–343, 2009.

[7] J Zou et al, "Split bregman algorithm for multiple measurement vector problem," *Multidim Syst Sign Process*, pp. 1–18, 2013.

[8] D Wei et al, "Group sparse optimization by alternating direction method," Tech. Rep., Dept. Comp. and App. Math., Rice U., 2011.